Neural Optimal Transport for Dynamical Systems

Methods and Applications in Biomedicine

Charlotte Bunne

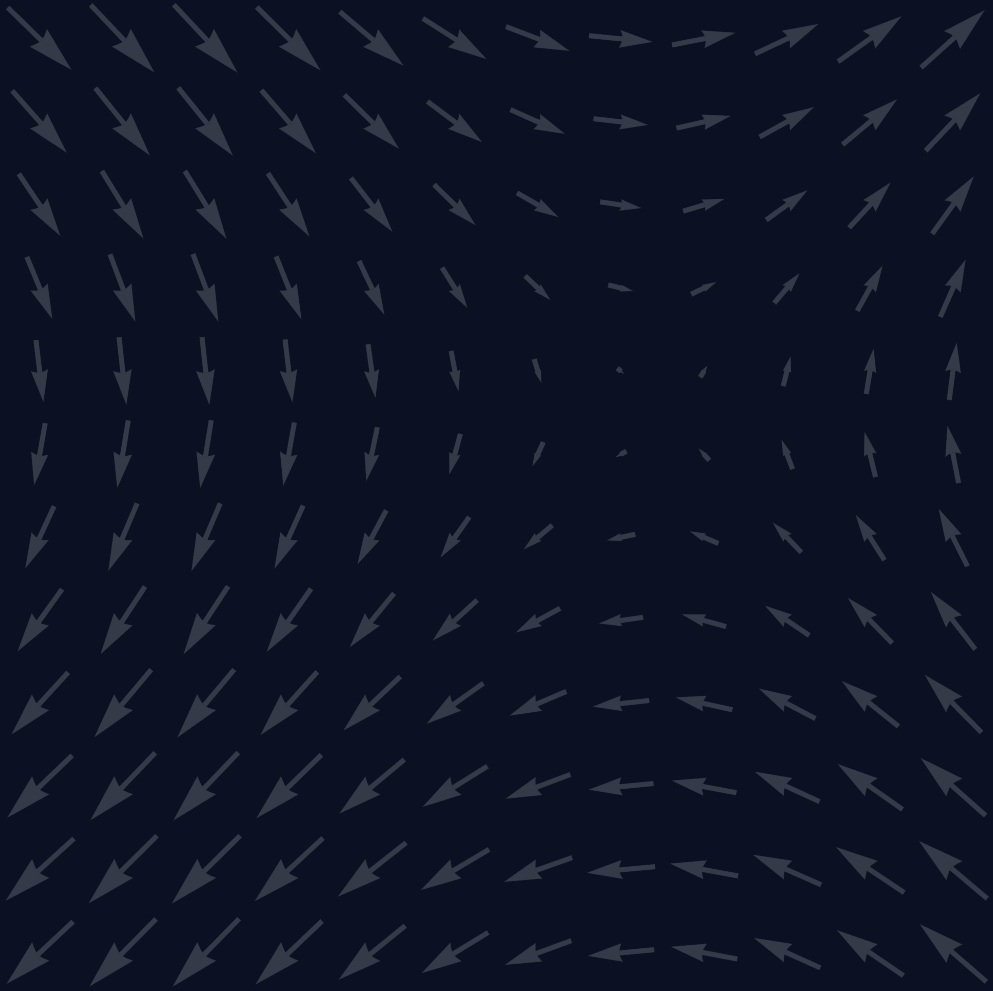

Diss.-No. ETH 29XXX

CHARLOTTE BUNNE

NEURAL OPTIMAL TRANSPORT FOR DYNAMICAL SYSTEMS

METHODS AND APPLICATIONS IN BIOMEDICINE

DISS. ETH NO. ?

NEURAL OPTIMAL TRANSPORT FOR DYNAMICAL SYSTEMS

METHODS AND APPLICATIONS IN BIOMEDICINE

A dissertation submitted to attain the degree of

DOCTOR OF SCIENCES of ETH ZURICH
(Dr. sc. ETH Zurich)

presented by

CHARLOTTE BUNNE
M. sc. ETH Zurich

born on 29 August 1995

accepted on the recommendation of

Prof. Dr. Andreas Krause, examiner
Prof. Dr. Marco Cuturi, co-examiner
Prof. Dr. Lucas Pelkmans, co-examiner
Prof. Dr. Jure Leskovec, co-examiner

2023

Charlotte Bunne: *Neural Optimal Transport for Dynamical Systems,* © 2023

DOI: 10.3929/ethz-a-

Und was in schwankender Erscheinung schwebt,
Befestiget mit dauernden Gedanken.
— Johann Wolfgang von Goethe, *Faust I* (1808)

ABSTRACT

English abstract here.

ZUSAMMENFASSUNG

Deutsche Zusammenfassung hier.

ACKNOWLEDGEMENTS

First and foremost, I would like to express my sincere gratitude to my advisors Andreas Krause and Marco Cuturi. ... I am very grateful to Anne Carpenter and Shantanu Singh, my mentors at the Broad Institute of MIT and Harvard. ... I will be forever grateful for this. Further, I would also like to thank ... and Jure Leskovec for being on my thesis committee, and for providing me with invaluable feedback. Aviv, in particular, ...

The thesis would not be the same without the longstanding collaboration with Lucas Pelkmans and Gabriele Gut. ...

I am profoundly indebted to other co-authors with whom I worked on many projects throughout the past years, in particular, Gunnar Rätsch, Stefan Stark, Ya-Ping Hsieh, Vignesh Ram Somnath, Frederike Lübeck, Matteo Pariset, Valentin De Bortoli, Octavian Ganea, Laetitia Meng-Papaxanthos, and Philippe Schwaller. Thank you especially to Ya-Ping Hsieh and Stefan Stark for hour-long discussions on various projects. ...

Further, I am very grateful for my first academic mentors, Stefanie Jegelka, David Alvarez Melis, Roland Eils, Thomas Höfer, and Lisa Buchauer. ... I would not have started my scientific journey without the Life-Science Lab of the German Cancer Research Center. It is what sparked my interest in biology and engineering. It ...

Thanks to all members of the Learning and Adaptive Systems group for creating an excellent research environment. In particular, my office mates Parnian Kassraie, Lars Lorch, and Jonas Rothfuss. Thank you, Rita Klute, for entangling the jungle of bureaucracy and never getting tired of my administrative requests.

I am very grateful to my parents Nele and Egon and siblings Kaspar, Henriette, and Frieder for there endless love, advice, and support. Lastly, I always wondered ... Pol, I cannot put in words what you mean to me.

CONTENTS

NOTATION

Σ_d Probability simplex of size d

ACRONYMS

BDT Black-Derman-Toy.
BM Brownian motion.

DDPM denoising diffusion probabilistic model.
DSB diffusion Schrödinger bridge.

GSB Gaussian Schrödinger bridge.

IPF iterative proportional fitting.

OT optimal transport.
OU Ornstein-Uhlenbeck.

SB Schrödinger bridge.
SDE stochastic differential equation.
SMLD score matching with Langevin dynamics.

VESDE variance exploding SDE.
VPSDE variance preserving SDE.

1

INTRODUCTION

...

— ..., ... (...)

(Bunne et al., 2021) optimal transport (OT)

2

OPTIMAL TRANSPORT FOR DYNAMICAL SYSTEMS

...

— ..., ... (...)

OPTIMAL TRANSPORT. For two probability measures μ, ν in $\mathcal{P}(\mathbb{R}^d)$, their squared 2-Wasserstein distance is

$$W_2^2(\mu,\nu) = \inf_{\gamma \in \Gamma(\mu,\nu)} \iint \|x-y\|_2^2 \gamma(dx,dy), \tag{2.1}$$

where $\Gamma(\mu,\nu)$ is the set of couplings on $\mathbb{R}^d \times \mathbb{R}^d$ with respective marginals μ, ν. When instantiated on finite discrete measures, such as $\mu = \sum_{i=1}^n a_i \delta_{x_i}$ and $\nu = \sum_{j=1}^m b_j \delta_{y_j}$, this problem translates to a linear program, which can be regularized using an entropy term (Cuturi, 2013; Peyré and Cuturi, 2019). For $\varepsilon \geq 0$, set

$$W_\varepsilon(\mu,\nu) := \min_{\mathbf{P} \in U(a,b)} \langle \mathbf{P}, [\|x_i - y_j\|^2]_{ij} \rangle - \varepsilon H(\mathbf{P}), \tag{2.2}$$

where $H(\mathbf{P}) := -\sum_{ij} \mathbf{P}_{ij}(\log \mathbf{P}_{ij} - 1)$ and the polytope $U(a,b)$ is the set of $n \times m$ matrices $\{\mathbf{P} \in \mathbb{R}_+^{n \times m}, \mathbf{P}\mathbf{1}_m = a, \mathbf{P}^\top \mathbf{1}_n = b\}$. Notice that the definition above reduces to the usual (squared) 2-Wasserstein distance when $\varepsilon = 0$. Setting $\varepsilon > 0$ yields a faster and differentiable proxy to approximate W_0, but introduces a bias, since $W_\varepsilon(\mu,\mu) \neq 0$ in general. In the rest of this work, we therefore use the *Sinkhorn divergence* (Ramdas et al., 2017; **?**; Salimans et al., 2018; Feydy et al., 2019) as a valid non-negative discrepancy,

$$\overline{W}_\varepsilon(\mu,\nu) := W_\varepsilon(\mu,\nu) - \frac{1}{2}\left(W_\varepsilon(\mu,\mu) + W_\varepsilon(\nu,\nu)\right). \tag{2.3}$$

OT AND CONVEXITY. An alternative formulation for OT is given by the Monge (1781) problem

$$W_2^2(\mu,\nu) = \inf_{T : T_\# \mu = \nu} \int_{\mathcal{X}} ||x - T(x)||^2 d\mu(x) \tag{2.4}$$

where # is the push-forward operator, and the optimal solution $T^\star$ is known as the Monge map between μ and ν. The Brenier theorem 1987 states that if

μ has a density, the Monge map $T^\star$ between μ and ν can be recovered as the gradient of a unique (up to constants) convex function ψ whose gradient pushes forward μ to ν. Namely, if $\psi : \mathbb{R}^d \to \mathbb{R}$ is convex and $(\nabla\psi)_\# \mu = \nu$, then $T^\star(x) = \nabla\psi(x)$ and

$$W_2^2(\mu, \nu) = \int_{\mathcal{X}} ||x - \nabla\psi(x)||^2 d\mu(x)\,. \tag{2.5}$$

3

DYNAMICAL PROCESSES IN BIOMEDICINE

The results suggest a helical structure (which must be very closely packed) containing probably 2, 3 or 4 coaxial nucleic acid chains per helical unit and having the phosphate groups near the outside.

— Rosalind Franklin, *Report* (1952)

Part I

STATIC NEURAL OPTIMAL TRANSPORT

4

...

Tout va par degré dans la nature, et rien par saut, et cette regle à l'égard des changements est une partie de ma loi de la continuité.
— Gottfried Wilhelm Leibniz, *Nouveaux essais sur l'entendement humain* (1765)

CONVEX NEURAL ARCHITECTURES. Input convex neural networks are neural networks $\psi_\theta(x)$ with specific constraints on the architecture and parameters θ, such that their output is a convex function of some (or all) elements of the input x (Amos et al., 2017). We consider in this work *fully* input convex neural networks (ICNNs), such that the output is a convex function of the entire input x. A typical ICNN is a L-layer, fully connected network such that, for $l = 0, \dots, L-1$:

$$z_{l+1} = a_l(W_l^x x + W_l^z z_l + b_l) \text{ and } \psi_\theta(x) = z_L, \tag{4.1}$$

where by convention, z_0 and W_0^z are 0, a_l are convex non-decreasing (non-linear) activation functions, $\theta = \{b_l, W_l^z, W_l^x\}_{l=0}^{L-1}$ are the weights and biases of the neural network, with weight matrices W_l^z associated to latent representations z that have non-negative entries. Since Amos et al. (2017)'s work, convex neural architectures have been further extended and shown to capture relevant models despite these constraints (Amos et al., 2017; **?**; Huang et al., 2021). In particular, Chen et al. (2019) provide a theoretical analysis that any convex function over a convex domain can be approximated in sup norm by an ICNN.

5

...

...

— ..., ... (...)

A key challenge in the treatment of cancer is to predict the effect of drugs, or a combination thereof, on cells of a particular patient. To achieve that goal, single-cell sequencing can now provide measurements for individual cells, in treated and untreated conditions, but these are, however, not in correspondence. Given such examples of untreated and treated cells under different drugs, can we predict the effect of new drug combinations? We develop a general approach motivated by this and related problems, through the lens of *optimal transport (OT) theory*, and, in that process, develop tools that might be of interest for other application domains of OT. Given a collection of N pairs of measures (μ_i, ν_i) over $\mathbb{R}^d$ (cell measurements), tagged with a context c_i (encoding the treatment), we seek to learn a context-dependent, parameterized transport map $\mathcal{T}_\theta$ such that, on training data, that map $\mathcal{T}_\theta(c_i) : \mathbb{R}^d \to \mathbb{R}^d$ fits the dataset, in the sense that $\mathcal{T}_\theta(c_i)\sharp\mu_i \approx \nu_i$. Additionally, we expect that this parameterized map can generalize to unseen contexts and patients, to predict, given a patient's cells described in μ_{new}, the effect of applying context c_{new} on these cells as $\mathcal{T}_\theta(c_{\text{new}})\sharp\mu$.

Learning Mappings Between Measures From generative adversarial networks, to normalizing flows and diffusion models, the problem of learning maps that move points from a source to a target distribution is central to machine learning. OT theory (Santambrogio, 2015) has emerged as a principled approach to carry out that task: For a pair of measures μ, ν supported on $\mathbb{R}^d$, OT suggests that, among all maps T such that ν can be reconstructed by applying T to every point in the support of μ (abbreviated with the push-forward notation as $T\sharp\mu = \nu$), one should favor so-called Monge maps, which *minimize* the average squared-lengths of displacements $\|x - T(x)\|^2$. A rich literature, covered in Peyré and Cuturi (2019), addresses computational challenges of estimating such maps, with impactful applications to various areas of science (cf., Hashimoto et al., 2016; Schmitz et al., 2018; Schiebinger et al., 2019a; Yang et al., 2020; Janati et al., 2020; Bunne et al., 2023).

Neural OT We focus in this work on neural approaches that parameterize the optimal maps T as neural networks. An early approach is the work on

Wasserstein GANs (Arjovsky et al., 2017), albeit the transport map is not explicitly estimated. Several recent results have exploited a more explicit connection between OT and NNs, derived from the celebrated Brenier theorem (1987), which states that Monge maps are necessarily gradients of convex functions. Such convex functions can be represented using input convex neural networks (ICNN) (Amos et al., 2017), to parameterize either the Monge map (Jacob et al., 2018; Yang and Uhler, 2019; Bunne et al., 2021, 2022b) or a dual potential (Makkuva et al., 2020; Korotin et al., 2020) as, respectively, the gradient of an ICNN or an ICNN itself. In this paper, we build on this line of work, but substantially generalize it, to learn a *parametric* family of context-aware transport maps, using a collection of labeled pairs of measures.

Contributions We propose a framework that can leverage *labeled* pairs of measures $\{(_i, (\mu_i, \nu_i))\}_i$ to infer a *global* parameterized map $\mathcal{T}_\theta$. Hereby, the context $_i$ belongs to an arbitrary set $\mathcal{C}$. We construct $\mathcal{T}_\theta$ so that it should be able, given a possibly unseen context label $\in$, to output a map $\mathcal{T}_\theta(c) : \mathbb{R}^d \to \mathbb{R}^d$, that is itself the gradient of a convex function. To that end, we propose to learn these parameterized Monge maps $\mathcal{T}_\theta$ as the gradients of partially input convex neural networks (PICNN), which we borrow from the foundational work of Amos et al. (2017). Our framework can be also interpreted as a hypernetwork (Ha et al., 2016): The PICNN architecture can be seen as an ICNN whose weights and biases are *modulated* by the context vector , which parameterizes a *family* of convex potentials in $\mathbb{R}^d$. Because both ICNN —and to a greater extent PICNN— are notoriously difficult to train (Richter-Powell et al., 2021; Korotin et al., 2020, 2021), we use closed-form solutions between Gaussian approximations to derive relevant parameter initializations for (P)ICNNs: These choices ensure that, *upon initialization*, the gradient of the (P)ICNNs mimics the affine Monge map obtained in closed form between Gaussian approximations of measures μ_i, ν_i (Gelbrich, 1990). Our framework is applied to three scenarios: Parameterization of transport through a real variable (time or drug dosage), through an auxiliary informative variable (cell covariates) and through action variables (genetic perturbations in combination) (see Fig. 8.1). Our results demonstrate the ability of our architectures to better capture on out-of-sample observations the effects of these variables in various settings, even when considering never-seen, composite context labels. These results suggest potential applications of conditional OT to model personalized medicine outcomes, or to guide novel experiments, where OT could serve as a predictor for never tested context labels.

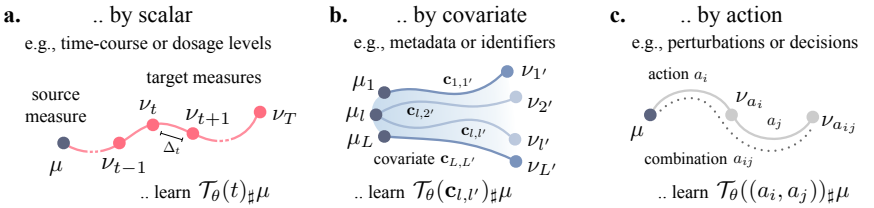

FIGURE 5.1: The evolution from a source μ to a target measure ν can depend on context variables c of various nature. This comprises **a.** scalars such as time or dosage t which determine the magnitude of an optimal transport, **b.** flow of measures into another one based on additional information (possibly different between μ and ν) stored in vectors $\mathbf{c}_{l,l'}$, or **c.** discrete and complex actions a_i, possibly in combination a_{ij}. We seek a unified framework to produce a map $\mathcal{T}_\theta(c)$ from any type of condition c.

5.1 SUPERVISED TRAINING OF CONDITIONAL MONGE MAPS

We are given a dataset of N pairs of measures, each endowed with a label, $(c_i, (\mu_i, \nu_i)) \in \mathcal{C} \times \mathcal{P}(\mathbb{R}^d)^2$. Our framework builds upon two pillars: (i.) we formulate the hypothesis that an optimal transport $T_i^\star$ (or, equivalently, the gradient of a convex potential $f_i^\star$) explains how measure μ_i was mapped to ν_i, given context c_i; (ii.) we build on the multi-task hypothesis (Caruana, 1997) that all of the N maps $T_i^\star$ between μ_i and ν_i share a common set of parameters, that are *modulated* by context informations c_i. These ideas are summarized in an abstract regression model described below.

5.1.1 *A Regression Formulation for Conditional OT Estimation*

$\theta \in \Theta \subset \mathbb{R}^r$, $\mathcal{T}_\theta$ describes a function that takes an input vector $c \in \mathcal{C}$, and outputs a *function* $\mathcal{T}_\theta(c) : \mathbb{R}^d \to \mathbb{R}^d$, as a hypernetwork would (Ha et al., 2016). Assume momentarily that we are given *ground truth* maps T_i, that describe the effect of context c_i on any measure, rather only pairs of measures (μ_i, ν_i). This is of course a major leap of faith, since even recovering an OT map $T^\star$ from two measures is in itself very challenging (Hütter and Rigollet, 2021; Rigollet and Stromme, 2022; Pooladian and Niles-Weed, 2021). If such maps were available, a direct supervised approach to learn a

unique θ could hypothetically involve minimizing a fit function composed of losses between maps

$$\min_{\theta} \sum_{i=1}^{N} \int_{\mathbb{R}^d} \|\mathcal{T}_\theta(c_i)(x) - T_i(x)\|^2 \, \mathrm{d}\mu_i(x) \,. \tag{5.1}$$

Unfortunately, such maps T_i are not given, since we are only provided unpaired samples before μ_i and after ν_i that map's application. By Brenier's theorem, we know, however, that such an OT map $T_i^\star$ exists, and that it would be necessarily the gradient of a convex potential function that maximizes (**??**). As a result, we propose to modify (5.1) to (i.) parameterize, for any c, the map $\mathcal{T}_\theta(c)$ as the gradient w.r.t. x of a function $f_\theta(x, c) : \mathbb{R}^d \times \mathcal{C} \to \mathbb{R}$ that is convex w.r.t. x, namely $\mathcal{T}_\theta(\,) := x \mapsto \nabla_1 f_\theta(x, \,)$; (ii.) estimate θ by maximizing *jointly* the dual objectives (**??**) simultaneously for all N pairs of measures, in order to ensure that the maps are close to optimal, to form the aggregate problem

$$\max_\theta \textstyle\sum_{i=1}^{N} \mathcal{E}_{\mu_i,\nu_i}(f_\theta(\,\cdot\,, c_i)). \tag{5.2}$$

We detail in App. **??** how the Legendre transforms that appear in the energy terms $\mathcal{E}_{\mu_i,\nu_i}$ are handled with an auxiliary function.

5.1.2 *Integrating Context in Convex Architectures*

We propose to incorporate context variables, in order to modulate a family of convex functions $f_\theta(x, c)$ using partially input convex neural networks (PICNN). PICNNs are neural networks that can be evaluated over a pair of inputs $(x, \,)$, but which are only required to be convex w.r.t. x. Given an input vector x and context vector , a K-layer PICNN is defined as $\psi_\theta(x, c) = z_K$, where, recursively for $0 \leq k \leq K-1$ one has

$$\begin{aligned} u_{k+1} &= \tau_k \left(V_k u_k + v_k \right), \\ z_{k+1} &= \sigma_k \left(W_k^z \left(z_k \circ [W_k^{zu} u_k + b_k^z]_+ \right) + \; W_k^x \left(x \circ (W_k^{xu} u_k + b_k^x) \right) + W_k^u u_k + b_k^u \right), \end{aligned} \tag{5.3}$$

where the PICNN is initialized as $u_0 =, z_0 = \mathbf{0}$, $\circ$ denotes the Hadamard elementwise product, and τ_k is any activation function. The parameters of the PICNN are then given by

$$\theta = \{V_k, W_k^z, W_k^{zu}, W_k^x, W_k^{xu}, W_k^u, v_k, b_k^z, b_k^x, b_k^u\}.$$

Similar to ICNNs, the convexity w.r.t. input variable x is guaranteed as long as activation functions σ_i are convex and non-decreasing, and the weight

matrices W_k^z have non-negative entries. We parameterize this by storing them as elementwise applications of softplus operations on precursor matrices of the same size, or, alternatively, by regularizing their negative part. Finally, much like ICNNs, all matrices at the $K-1$ layer are line vectors, and their biases scalars.

Such networks were proposed by Amos et al. (2017, Eq. 3) to address a problem that is somewhat symmetric to ours: Their inputs were labeled as (y, x), where y is a label vector, typically much smaller than that of vector x. Their PICNN is convex w.r.t. y, in order to easily recover, given a datapoint x (e.g., an image) the best label y that corresponds to x using gradient descent as a subroutine, i.e. $y^\star(x) = \arg\min_y \text{PICNN}_\theta(x, y)$. PICNN were therefore originally proposed to learn a parameterized, implicit classification layer, amortized over samples, whose motivation rests on the property that it is convex w.r.t. label variable y. By contrast, we use PICNNs that are convex w.r.t. data points x. In addition to that swap, we do not use the convexity of the PICNN to define an implicit layer (or to carry out gradient descent). Indeed, it does not make sense in our setting to minimize $\psi_\theta(x,)$ as a function of x, since x is an observation. Instead, our work rests on the property that $\nabla_1 \psi_\theta(x,)$ describes a parameterized family of OT maps. We note that PICNNs were considered within the context of OT in (Fan et al., 2021, Appendix B). In that work, PICNN provide an elegant reformulation for neural Wasserstein barycenters. Fan et al. (2021) considered a context vector c that was restricted to be a small vector of probabilities.

5.1.3 *Conditional Monge Map Architecture*

Using PICNNs as a base module, the CondOT architecture integrates operations on the contexts . As seen in Figure 8.1, context values may take various forms:

1. A scalar t denoting a strength or a temporal effect. For instance, McCann's interpolation and its time parameterization, $\alpha_t = ((1-t)\text{Id} + tT)_\sharp \alpha_0$ (McCann, 1997) can be interpreted as a trivial conditional OT model that creates, from an OT map ψ_θ, a set of maps parameterized by t, $\mathcal{T}_\theta(t) := x \mapsto \nabla_x \left((1-t)\|x\|^2/2 + t\psi_\theta(x)\right)$.
2. A covariate vector influencing the nature of the effect that led μ_i to ν_i, (capturing, e.g., patient feature vectors).
3. One or multiple actions, possibly discrete, representing decisions or perturbations applied onto μ_i.

To provide a flexible architecture capable of modeling different types of conditions as well as conditions appearing in combinations, the more general CondOT architecture consists of the hypernetwork $\mathcal{T}_\theta$ that is fed a context vector through embedding and combinator modules. This generic architecture provides a one-size fits all approach to integrate all types of contexts .

EMBEDDING MODULE To give greater flexibility when setting the context variable c, CondOT contains an embedding module $\mathcal{E}$ that translates arbitrary contexts into real-valued vectors. Besides simple scalars t (Fig. 8.1a) for which no embedding is required, discrete contexts can be handled with an embedding module $\mathcal{E}_\phi$. When the set is small, this can be done effectively using one-hot embeddings $\mathcal{E}_{\text{ohe}}$. For more complicated actions a such as treatments, there is no simple way to vectorize a context c. Similarly to action embeddings in reinforcement learning (Chandak et al., 2019; Tennenholtz and Mannor, 2019), we can learn embeddings for discrete actions into a learned continuous representation. This often requires domain-knowledge on the context values. For molecular drugs, for example, we can learn molecular representations $\mathcal{E}_{\text{mol}}$ such as chemical, motif-based (Rogers and Hahn, 2010) or neural fingerprints (Rong et al., 2020; Schwaller et al., 2022). However, often this domain knowledge is not available. In this work, we thus construct so-called *mode-of-action* embeddings, by computing an embedding $\mathcal{E}_{\text{moa}}$ that encourages actions a with similar effect on target population ν to have a similar representation. In § 8.3, we analyze several embedding types for different use-cases.

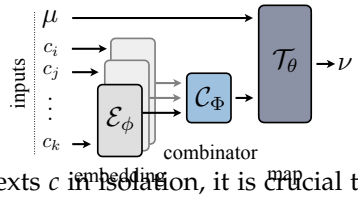

COMBINATOR MODULE While we often have access to contexts c in isolation, it is crucial to infer the effect of contexts applied in combination. A prominent example are cancer combination therapies, in which multiple treatment modalities are administered in combination to enhance treatment efficacy (Kummar et al., 2010). In these settings, the mode of operation between individual contexts c is often not known, and can thus not be directly modeled via simple arithmetic operations such as `min, max, sum, mean`. While we test as a baseline the case, applicable to one-hot-embeddings, where simple additions are used to model these combinations, we propose to augment the CondOT

Method	Conditioned on Drug Dosage				Conditioned on Cell Line	
	In-Sample		Out-of-Sample		In-Sample	
	MMD	ℓ_2(PS)	MMD	ℓ_2(PS)	MMD	ℓ_2(PS)
CPA (Lotfollahi et al., 2021)	0.1502 ± 0.0769	2.47 ± 2.89	0.1568 ± 0.0729	2.65 ± 2.75	0.2551 ± 0.006	2.71 ± 1.51
ICNN OT (Makkuva et al., 2020)	0.0365 ± 0.0473	2.37 ± 2.15	0.0466 ± 0.0479	2.24 ± 2.39	0.0206 ± 0.0109	1.16 ± 0.75
CondOT (Identity initialization)	0.0111 ± 0.0055	0.63 ± 0.09	0.0374 ± 0.0052	2.02 ± 0.10	0.0148 ± 0.0078	0.39 ± 0.06
CondOT (Gaussian initialization)	0.0128 ± 0.0081	0.60 ± 0.11	0.0325 ± 0.0062	1.84 ± 0.14	0.0146 ± 0.0074	0.41 ± 0.07

TABLE 5.1: Evaluation of drug effect predictions from control cells to cells treated with drug Givinostat when conditioning on various covariates influencing cellular responses such as drug dosage and cell type. Results are reported based on MMD and the ℓ_2 distance between perturbation signatures of marker genes in the 1000 dimensional gene expression space.

architecture with a parameterized combinator module $\mathcal{C}_\Phi$. If the order in which the actions are applied is irrelevant or unknown, the corresponding network $\mathcal{C}_\Phi$ needs to be permutation-invariant, which can be achieved by using a deep set architecture (Zaheer et al., 2017). Receiving a flexible number of inputs from the embedding module $\mathcal{E}_\phi$, CondOT allows for a joint training of the PICNN parameters θ, embedding parameters ϕ, and combinator parameters Φ in a single, end-to-end differentiable architecture.

TRAINING PROCEDURE Given a dataset $\mathcal{D} = \{c_i, (\mu_i, \nu_i)\}_{i=0}^N$ of N pairs of populations before μ_i and after transport ν_i connected to a context c_i, we detail in Algorithm **??** provided in § **??**, a training loop that incorporates all of the architecture proposals described above. The training loss aims at making sure the map $\mathcal{T}_\theta(c_i)$ is an OT map from μ_i to ν_i, where c_i may either be the original label itself or its embedded/combined formulation in more advanced tasks. To handle the Legendre transform in (**??**), we use the proxy dual objective defined in (Makkuva et al., 2020, Eq. 6) (**??**)-(**??**) in place of (**??**) in our overall loss (5.2). This involves training the CondOT architecture using two PICNNs, i.e., PICNN_{θ_f} and PICNN_{θ_g}, that share the same embedding/combinator module, with a regularization (**??**) promoting that for any c, the $\text{PICNN}_{\theta_g}(\cdot, c)$ resembles the Legendre transform of the other, $\text{PICNN}^*_{\theta_f}(\cdot, c)$.

5.2 EVALUATION

Biological cells undergo changes in their molecular profiles upon chemical, genetic, or mechanical perturbations. These changes can be measured using recent technological advancements in high-resolution multivariate

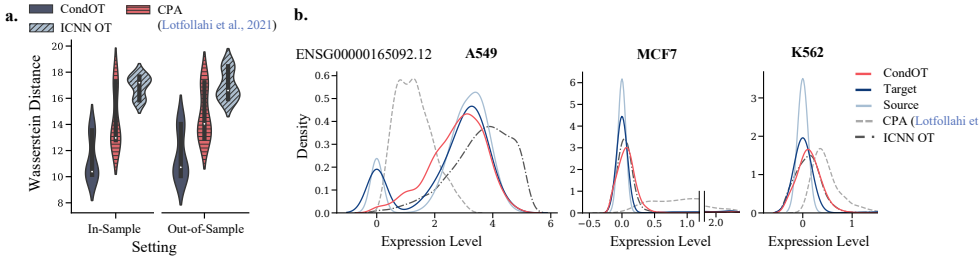

FIGURE 5.2: **a.** Predictive performance of CONDOT and baselines w.r.t. the entropy-regularized Wasserstein distance on drug dosages *in-sample*, i.e., seen during training, and *out-of-sample*, i.e., unseen during training. **b.** Marginal distributions of observed source and target distributions, as well as predictions on perturbed distributions by CONDOT and baselines of an exemplary gene across different cell lines. Predicted marginals of each method should match the marginal of the target population.

single-cell biology. Measuring single cells in their unperturbed or perturbed state requires, however, to destroy them, resulting in populations μ and ν that are unpaired. The relevance of OT to that comes from its ability to resolve such ambiguities through OT maps, holding promises of a better understanding of health and disease. We consider various high-dimensional problems arising from this scenario to evaluate the performance of CONDOT (§ 5.1) versus other baselines.

5.2.1 *Population Dynamics Conditioned on* Scalars

Upon application of a molecular drug, the state of each cell x_i of the unperturbed population is altered, and observed in population ν. Molecular drugs are often applied at different dosage levels t, and the magnitude of changes in the gene expression profiles of single cells highly correlates with that dosage. We seek to learn a global, parameterized transport map $\mathcal{T}_\theta$ sensitive to that dosage.We evaluate our method on the task of inferring single-cell perturbation responses to the cancer drug Givinostat, a histone deacetylase inhibitor with potential anti-inflammatory, anti-angiogenic, and antineoplastic activities (Srivatsan et al., 2020), applied at different dosage levels, i.e., $t \in \{10\,\text{nM}, 100\,\text{nM}, 1,000\,\text{nM}, 10,000\,\text{nM}\}$. The dataset contains 3,541 cells described with the gene expression levels of 1,000 highly-variable genes. In

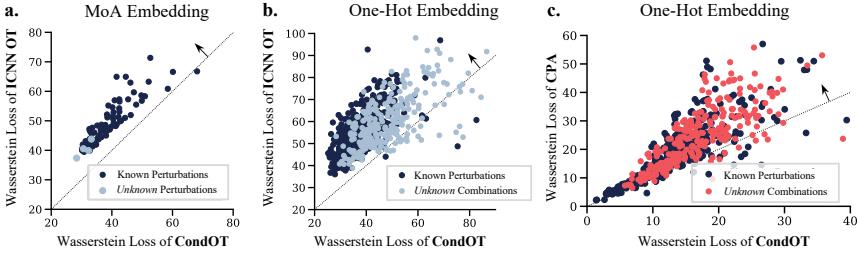

FIGURE 5.3: Comparison between **a.** CONDOT and ICNN OT (Makkuva et al., 2020) based on embedding $\mathcal{E}_{\text{moa}}$ **b.** as well as $\mathcal{E}_{\text{ohe}}$, and **c.** CONDOT and CPA (Lotfollahi et al., 2021) based on embedding $\mathcal{E}_{\text{ohe}}$ on *known* and *unknown* perturbations or combinations. Results above the diagonal suggest higher predictive performance of CONDOT.

a first experiment, we measure how well CONDOT captures the drug effects at different dosage levels via distributional distances such as MMD (Gretton et al., 2012) and the ℓ_2-norm between the corresponding perturbation signatures (PS), as well as the entropy-regularized Wasserstein distance (Cuturi, 2013). We compute the metrics on 50 marker genes, i.e., genes mostly affected upon perturbation. For more details on evaluation metrics, see § **??**. To put CONDOT's performance into perspective, we compare it to current state-of-the-art baselines (Lotfollahi et al., 2021) as well as parameterized Monge maps without context variables (Bunne et al., 2021; Makkuva et al., 2020, ICNN OT), see § **??**. As visible in Table 5.1 and Fig. 5.2a, CONDOT achieves consistently more accurate predictions of the target cell populations at different dosage levels than OT approaches that cannot utilize context information, demonstrated through a lower average loss and a smaller variance. This becomes even more evident when moving to the setting where the population has been trained only on a subset of dosages and we test CONDOT on *out-of-sample* dosages. Table 5.1 and Fig. 5.2a demonstrate that CONDOT is able to generalize to previously *unknown* dosages, thus learning to interpolate the perturbation effects from dosages seen during training. For further analysis, we refer the reader to § **??** (see Fig. **??** and **??**). We further provide an additional comparison of CONDOT, operating in the multi-task setting, to the single-task performance of optimal transport-based methods § **??**. While the single-task setting of course fails to generalize to new contexts and requires all contexts to be distinctly known, it provides us with a *pseudo* lower bound, which CONDOT is able to reach (see Table **??**).

5.2.2 *Population Dynamics Conditioned on* Covariates

Molecular processes are often highly dependent on additional covariates that steer experimental conditions, and which are not present in the features measures in population μ or ν. This can be, for instance, factors such as different cell types clustered within the populations. When the model can only be conditioned w.r.t. a small and *fixed* set of metadata information, such as cell types, it is sufficient to encode these contexts using a one-hot embedding module $\mathcal{E}_{\text{ohe}}$. To illustrate this problem, we consider cell populations comprising three different cell lines (A549, MCF7, and K562). As visible in Table 5.1, CondOT outperforms current baselines which equally condition on covariate information such as CPA (Lotfollahi et al., 2021), assessed through various evaluation metrics. Figure 5.2b displays a gene showing highly various responses towards the drug Givinostat dependent on the cell line. CondOT captures the distribution shift from control to target populations consistently across different cell lines.

5.2.3 *Population Dynamics Conditioned on* Actions

To recommend personalized medical procedures for patients, or to improve our understanding of genetic circuits, it is key to be able to predict the outcomes of novel perturbations, arising from combinations of drugs or of genetic perturbations. Rather than learning individual maps T_θ^a predicting the effect of individual treatments, we aim at learning a global map $\mathcal{T}_\theta$ which, given as input the unperturbed population μ as well as the action a of interest, predicts the cell state perturbed by a. Thanks to its modularity, CondOT can not only learn a map T_θ for all actions *known* during training, but also to generalize to *unknown* actions, as well as potential *combinations* of actions. We will discuss all three scenarios below.

5.2.3.1 *Known Actions*

In the following, we analyze CondOT's ability to accurately predict phenotypes of genetic perturbations based on single-cell RNA-sequencing pooled CRISPR screens (Norman et al., 2019; Dixit et al., 2016), comprising 98,419 single-cell gene expression profiles with 92 different genetic perturbations, each cell measured via a 1,500 highly-variable gene expression vector. As, in a first step, we do not aim at generalizing beyond perturbations encountered during training, we utilize again a one-hot embedding $\mathcal{E}_{\text{ohe}}$ to condition $\mathcal{T}_\theta$ on each perturbation a. We compare our method to other

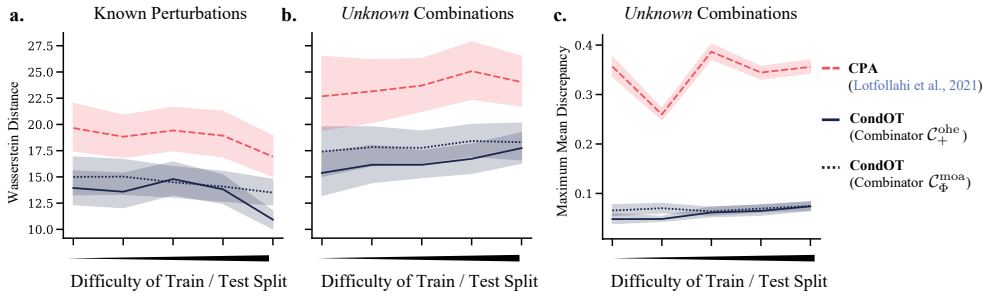

FIGURE 5.4: Predictive performance for **a.** known perturbations, **b.** unknown perturbations in combination w.r.t. regularized Wasserstein distance and **c.** MMD over different train / test splits of increasing difficulty for baseline CPA as well as CONDOT with different combinators $\mathcal{C}_{+}^{\text{ohe}}$ and $\mathcal{C}_{\Phi}^{\text{moa}}$. For more details on the dataset splits, see §**??**.

baselines capable of modeling effects of a large set of perturbations such as CPA (Lotfollahi et al., 2021). Often, the effect of genetic perturbations are subtle in the high-dimensional gene expression profile of single cells. Using ICNN-parameterized OT maps without context information, we can thus assess the gain in accuracy of predicting the perturbed target population by incorporating context-awareness over simply predicting an average perturbation effect. Figure 5.3a and b demonstrate that compared to OT ablation studies, Fig. 5.3c and Fig. 5.4a for the current state-of-the-art method CPA (Lotfollahi et al., 2021). Compared to both, CONDOT captures the perturbation responses more accurately w.r.t. the Wasserstein distance.

5.2.3.2 *Unknown Actions*

With the emergence of new perturbations or drugs, we aim at inferring cellular responses to settings not explored during training. One-hot embeddings, however, do not allow us to model *unknown* perturbations. This requires us to use an embedding $\mathcal{E}$, which can provide us with a representation of an unknown action a'. As genetic perturbations further have no meaningful embeddings as, for example, molecular fingerprints for drugs, we resort to mode-of-action embeddings introduced in § 5.1.3. Assuming marginal sample access to all individual perturbations, we compute a multidimensional scaling (MDS)-based embedding from pairwise Wasserstein distances between individual target populations, such that perturbations with similar effects are closely represented. For details, see § **??**. As current

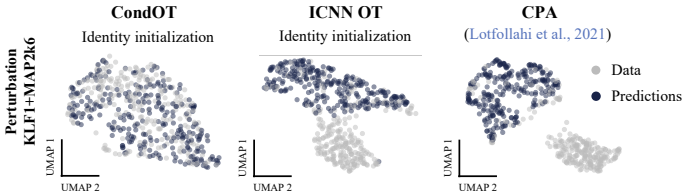

FIGURE 5.5: UMAP embeddings of cells perturbed by the combination KLF1+MAP2K6 (gray) and predictions of CONDOT (ours), ICNN OT (Makkuva et al., 2020), and CPA (blue). While CONDOT aligns well with observed perturbed cells, the baselines fail to capture subpopulations.

state-of-the-art methods are restricted to modeling perturbations via one-hot encodings, we compare our method to ICNN OT only. As displayed in Fig. 5.3a, CONDOT accurately captures the response of *unknown* actions (BAK1, FOXF1, MAP2K6, MAP4K3), which were not seen during training, at a similar Wasserstein loss as perturbation effects seen during training. For more details, see § **??**.

5.2.3.3 *Actions in Combination*

While experimental studies can often measure perturbation effects in biological systems in isolation, the combinatorial space of perturbations in composition is too large to capture experimentally. Often, however, combination therapies are cornerstones of cancer therapy (Mokhtari et al., 2017). In the following, we test different combinator architectures to predict genetic perturbations in combination from single targets. Similarly to Lotfollahi et al. (2021), we can embed combinations by adding individual one-hot encodings of single perturbations (i.e., $\mathcal{C}_{+}^{\text{ohe}}$). In addition, we parameterize a combinator via a permutation-invariant deep set, as introduced in § 5.1.3, based on mode-of-action embeddings of individual perturbations (i.e., $\mathcal{C}_{\Phi}^{\text{moa}}$). We split the dataset into train / test splits of increasing difficulty (details on the dataset splits in §**??**). Initially containing all individual perturbations as well as some combinations, the number of perturbations seen in combination during training decreases over each split. For more details, see § **??**. We compare different combinators to ICNN OT (Fig. 5.3b) and CPA (Lotfollahi et al., 2021) (Fig. 5.3c, Fig. 5.4b, c). While the performance drops compared to inference on *known* perturbations (Fig. 5.4a) and decreases with increasing difficulty of the train / test split, CONDOT outperforms all baselines.

When embedding these high-dimensional populations in a low-dimensional UMAP space (McInnes et al., 2018), one can see that CondOT captures the entire perturbed population, while ICNN OT and CPA fail in capturing certain subpopulations in the perturbed state (see Fig. 5.5 and **??**).

5.3 CONCLUSION

We have developed the CondOT framework that is able to infer OT maps from not only one pair of measures, but many pairs that come labeled with a context value. To ensure that CondOT encodes optimal transports, we parameterize it as a PICNN, an input-convex NN that modulates the values of its weights matrices according to a sequence of feature representations of that context vector. We showcased the generalization abilities of CondOT in the extremely challenging task of predicting outcomes for unseen combinations of treatments. These abilities and PICNN more generally hold several promises, both as an augmentation of the `OTT` toolbox (Cuturi et al., 2022), and for future applications of OT to single-cell genomics.

Part II

DYNAMIC NEURAL OPTIMAL TRANSPORT

6

...

Living matter evades the decay to equilibrium.
— Erwin Schrödinger, *What is Life?* (1944)

The Schrödinger bridge (SB) (**?**Chen et al., 2021b), alternatively known as the *dynamic* entropy-regularized optimal transport (OT), has recently received significant attention from the machine learning community. In contrast to the classical *static* OT where one seeks a coupling between measures that minimizes the average cost (Villani, 2009; **?**), the goal of SBs is to find the optimal *stochastic processes* that evolve a given measure into another. As such, SBs are particularly suitable for learning complex continuous-time systems, and have been successfully applied to a wide range of applications such as sampling (**??**), generative modeling (Chen et al., 2022a; De Bortoli et al., 2021; **?**), molecular biology (Holdijk et al., 2022), and mean-field games (Liu et al., 2022).

Despite of these impressive achievements, a common limitation of the existing works is that the SBs are typically solved in a purely numerical fashion. In sharp contrast, it is well-known that many important OT problems for *Gaussian* measures admit *closed-form* solutions, and the advantages of such solutions are numerous: they have inspired new learning methods (**???**), they can serve as the ground truth for evaluating numerical schemes (**?**), and they have lead to the discovery of a new geometry that is both rich in theory and application (**?**).

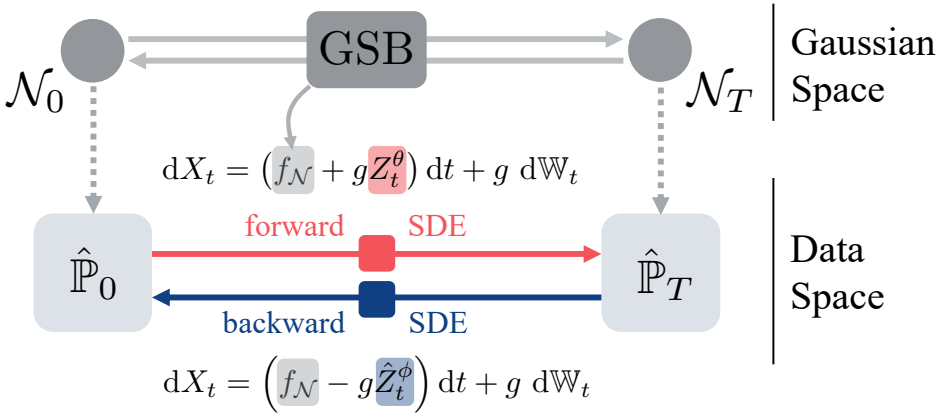

FIGURE 6.1: Solving the SB problem between $\hat{\mathbb{P}}_0$ and $\hat{\mathbb{P}}_1$ is notoriously difficult because it requires learning the time-dependent drifts of two SDEs that respect the desired marginals, and a random initialization for these drifts is usually extremely far from satisfying that constraint. We propose a data-dependent procedure that relies first on Gaussian approximations of the data measures, which provide a closed-form drift $f_{\mathcal{N}}$ in (6.29) (the GSB). We show that this facilitates the training of forward/backward drifts $\hat{Z}_t^\theta, \hat{Z}_t^\phi$.

The goal of our paper is to continue this pursuit of closed-form solutions and thereby extending these advantages to SB-based learning methods. For an overview of the method, see Fig. 8.1. To this end, we make the following **contributions**:

1. As our central result, we derive the closed-form expressions for Gaussian Schrödinger bridges (GSBs), i.e.,SBs between Gaussian measures. This is a challenging task for which all existing techniques fail, and thus we need to resort to a number of new ideas from entropic OT, Riemannian geometry, and generator theory; see **??**.
2. We extend the deep connection between geometry and Gaussian OT to Gaussian Schrödinger bridges. In particular, our results can be seen as a vast generalization of the classical Bures-Wasserstein geodesics between Gaussian measures (**??**), which is the foundation of many computational methods (**???**).
3. Via a simple Gaussian approximation on real *single-cell genomics* data, we numerically demonstrate that many benefits of the closed-form expressions in static OT immediately carry over to SB-based learning methods: We report improved numerical stability and tuning insensitivity when trained on benchmark datasets, which ultimately lead to an overall better performance.

6.1 PRELIMINARIES ON GAUSSIAN OPTIMAL TRANSPORT PROBLEMS

Throughout this paper, let $\xi \sim \mathcal{N}(\mu, \Sigma)$ and $\xi' \sim \mathcal{N}(\mu', \Sigma')$ denote two given Gaussian random variables. By abusing the notation, we will continue to denote the measures of these Gaussians by ξ and ξ', respectively. We will also denote by $\Pi(\xi, \xi')$ the set of all their couplings.

6.1.1 *Static Gaussian Optimal Transport*

The *static* entropy-regularized OT between Gaussians refers to the following minimization problem (**?**):

$$\min_{\pi \in \Pi(\xi, \xi')} \int \|x - x'\|^2 \mathrm{d}\pi(x, x') + 2\sigma^2 D_{\mathrm{KL}} \pi \xi \otimes \xi', \tag{6.1}$$

where $\xi \otimes \xi'$ denotes the product measure of ξ and ξ', and $\sigma \geq 0$ is a regularization parameter. When $\sigma = 0$, (6.1) reduces to the classical 2-Wasserstein distance between ξ and ξ' (Villani, 2009), whose closed-form

solution is classical (Dowson and Landau, 1982; **?**). The case for general σ is more involved, and an analytical expression was only recently found (**????**): Setting

$$D_\sigma := (4\Sigma^{\frac{1}{2}}\Sigma'\Sigma^{\frac{1}{2}} + \sigma^4 I)^{\frac{1}{2}}, \quad C_\sigma := \frac{1}{2}(\Sigma^{\frac{1}{2}} D_\sigma \Sigma^{-\frac{1}{2}} - \sigma^2 I), \tag{6.2}$$

then the solution $\pi^\star$ to (6.1) is itself a Gaussian:

$$\pi^\star \sim \mathcal{N}\left(\begin{bmatrix}\mu \\ \mu'\end{bmatrix}, \begin{bmatrix}\Sigma & C_\sigma \\ C_\sigma^\top & \Sigma'\end{bmatrix}\right). \tag{6.3}$$

6.1.2 *Dynamic Gaussian Optimal Transport*

In the literature, (6.1) is commonly referred to as the *static* OT formulation, since it merely asks *where* the mass should be transported to (i.e., $\pi(x, x')$ dictates how much mass at x should be transported to x'). In contrast, the more general problem of *dynamic* Gaussian OT seeks to answer *how* the mass the should be transported:

$$\min_{\rho_0=\xi,\ \rho_1=\xi'} \mathbb{E}\left[\int_0^1 \frac{1}{2}\|v_t\|^2 + \frac{\sigma^4}{8}\|\nabla \log \rho_t\|^2 \,\mathrm{d}t\right]. \tag{6.4}$$

Here, the minimization is taken over all pairs (ρ_t, v_t) where ρ_t is an absolutely continuous curve of measures (Ambrosio et al., 2006), and $v_t : \mathbb{R}^d \to \mathbb{R}^d$ is such that the continuity equation holds:

$$\partial_t \rho_t = -\nabla_x \cdot (\rho_t v_t), \tag{6.5}$$

where $(\nabla_x \cdot v_t)(x) := \sum_{i=1}^d \frac{\partial}{\partial x_i} v_t^i(x)$ denotes the divergence operator with respect to the x variable. It can be shown that, if $\rho_t^\star$ is the optimal curve for (6.4), then the joint distribution of the end marginals $(\rho_0^\star, \rho_1^\star)$ coincides with (6.3), hence the interpretation of $\rho_t^\star$ as the optimal *trajectory* in the space of measures (**??**Chen et al., 2021b; **?**).

To our knowledge, the only work that has partially addressed the closed-form solution of (6.4) is **?**, whose results are nonetheless insufficient to cover important applications such as generative modeling. In **??**, we will derive a vast generalization of the results in **?** and provide a detailed comparison in **??**–**??**.

6.2 THE GAUSSIAN SCHRÖDINGER BRIDGE PROBLEM AND ANALYSIS OVERVIEW

The purpose of this section is to introduce the core objectives in our paper, the Gaussian Schrödinger bridges, and establish their connection to the Gaussian OT problems in **??**. To help the reader navigate our somewhat technical proofs in **??**–**??**, we illustrate in section 6.2.2 the high-level challenges as well as our new techniques for solving Gaussian Schrödinger bridges.

6.2.1 *Schrödinger Bridges as Dynamic Entropy-Regularized Optimal Transport*

Let ν, ν' be two given measures and let $\mathbb{Q}_t$ be an arbitrary stochastic process. In its most generic form, the Schrödinger bridge refers to the following constrained KL-minimization problem over all stochastic processes $\mathbb{P}_t$ (**?**Chen et al., 2021b):

$$\min_{\mathbb{P}_0=\nu,\, \mathbb{P}_1=\nu'} D_{\mathrm{KL}}\mathbb{P}_t\mathbb{Q}_t. \tag{6.6}$$

In practice, ν and ν' typically arise as the (empirical) *marginal* distributions of a complicated continuous-time dynamics observed at the starting and end times, and $\mathbb{Q}_t$ is a "prior process" representing our belief of the dynamics before observing any data. The solution $\mathbb{P}_t^\star$ to (SB) is thus interpreted as the best dynamics that conforms to the prior belief $\mathbb{Q}_t$ while respecting the data marginals ($\mathbb{P}_0^\star = \nu, \mathbb{P}_1^\star = \nu'$).

In this paper, we will consider a general class of $\mathbb{Q}_t$'s that includes most existing processes in the machine learning applications of SBs. Specifically, with some initial condition Y_0, we will take $\mathbb{Q}_t$ to be the measure of the linear stochastic differential equation (SDE):

$$\mathrm{d}Y_t = (c_t Y_t + \alpha_t)\,\mathrm{d}t + g_t\,\mathrm{d}\mathbb{W}_t := f_t\,\mathrm{d}t + g_t\,\mathrm{d}\mathbb{W}_t. \tag{6.7}$$

Here, $c_t : \mathbb{R}^+ \to \mathbb{R}$, $\alpha_t : \mathbb{R}^+ \to \mathbb{R}^d$, and $g_t : \mathbb{R}^+ \to \mathbb{R}^+$ are smooth functions. In this case, SBs can be seen as generalized dynamical OT between two (not necessarily Gaussian) measures:

Theorem 1 *Consider the Schrödinger bridge problem with Y_t as the reference process:*

$$\min_{\mathbb{P}_0=\nu,\, \mathbb{P}_1=\nu'} D_{\mathrm{KL}}\mathbb{P}_t Y_t. \tag{6.8}$$

Then (6.8) is equivalent to

$$\inf_{(\rho_t, v_t)} \mathbb{E}\left[\int_0^1 \frac{\|v_t\|^2}{2g_t^2} + \frac{g_t^2}{8}\|\nabla \log \rho_t\|^2 - \frac{1}{2}\langle f_t, \nabla \log \rho_t\rangle \, \mathrm{d}t\right] \tag{6.9}$$

where the infimum is taken all pairs (ρ_t, v_t) *such that* $\rho_0 = \nu, \rho_1 = \nu'$, ρ_t *absolutely continuous, and*

$$\partial_t \rho_t = -\nabla_x \cdot (\rho_t(f_t + v_t)). \tag{6.10}$$

The proof of theorem 1, which we defer to **??**, is a straightforward extension of the argument in (**???**) which establishes the equivalence when Y_t is a reversible Brownian motion, i.e., $f_t \equiv 0, g_t \equiv \sigma$, and Y_0 follows the Lebesgue measure.[1]

6.2.2 *The Gaussian Schrödinger Bridge Problem*

The central goal of our paper is to derive the closed-form solution of SBs when the marginal constraints are Gaussians $\xi \sim \mathcal{N}(\mu, \Sigma)$, $\xi' \sim \mathcal{N}(\mu', \Sigma')$. Namely, we are interested in the following class of the SBs, termed Gaussian Schrödinger bridges:

$$\min_{\mathbb{P}_0 = \xi,\, \mathbb{P}_1 = \xi'} D_{\mathrm{KL}} \mathbb{P}_t Y_t. \tag{GSB}$$

To emphasize the dependence on the reference SDE, we will sometimes call (GSB) the Y_t-GSB.

Technical challenges; related work. In order to analyze (GSB), we first notice that the objective in (6.9) becomes $\sigma^{-2}\,\mathbb{E}\left[\int_0^1 \frac{1}{2}\|v_t\|^2 + \frac{\sigma^4}{8}\|\nabla \log \rho_t\|^2 \, \mathrm{d}t\right]$ for $\sigma \mathbb{W}_t$-GSBs. Up to a constant factor, this is simply (6.4), so theorem 1 reduces to the well-known fact that $\sigma \mathbb{W}_t$-GSBs are a reformulation of the dynamic Gaussian OT (**???**).

At first sight, this might suggest that one can extend existing tools in Gaussian OT to analyze GSBs. Unfortunately, the major difficulty of tackling GSBs is that these existing tools are fundamentally insufficient for the generalized objective (6.9). To be more precise, there exist three prominent frameworks for studying Gaussian OT problems:

- **Convex analysis:** An extremely fruitful observation in the field is that many Gaussian OT instances can be reduced to a *convex* program, for

1 The reversible Brownian motion is a technical construct to simplify the computations. For our purpose, one can think of $Y_0 \sim \xi$ instead of the Lebesgue measure, and our results still hold verbatim.

which one can import various convex techniques such as KKT or fixed-point arguments. This is the case for static Gaussian OT (6.1), both when $\sigma = 0$ (Dowson and Landau, 1982; **?**; **?**) and $\sigma > 0$ (**?**). Furthermore, in the case of $\sigma = 0$, the solution to the dynamic formulation (6.4) can be recovered from the static one via a simple linear interpolation (McCann, 1997).

- **Ad hoc computations:** When $\sigma > 0$ in (6.4), the problem is no longer reducible to a convex program (**?**Chen et al., 2021b). In this case, the only technique we are aware of is the ad hoc approach of (**?**), which manages to find a closed form for (6.4) (and thus $\sigma\mathbb{W}_t$-GSBs) through a series of brute-force computations.
- **Control theory:** On a related note, in a series of papers, **??**Chen et al. (2019) exploit the deep connection between $\sigma\mathbb{W}_t$-GSBs and control theory to study the *existence* and *uniqueness* of the solutions. Although a variety of new optimality conditions are derived in these works, they are all expressed in terms differential equations with coupled initial conditions, and it is unclear whether solving these differential equations is an easier task than (GSB) itself. In particular, no closed-form, even for $\sigma\mathbb{W}_t$-GSBs, can be found therein.

By theorem 1, GSBs are more general than (6.4) and thus irreducible to convex programs, so there is no hope for the convex route. As for ad hoc computations, the time-dependent f_t and g_t terms in (6.9) present a serious obstruction for generalizing the approach of **?** to Y_t-GSBs when $f_t \neq 0$ or g_t is not constant; this is exemplified by the convoluted expressions in our theorem 3, which hopefully will convince the reader that they are beyond any ad hoc guess. Finally, the control-theoretic view has so far fallen short of producing closed-form solutions even for $\sigma\mathbb{W}_t$-GSBs, so it is essentially irrelevant for our purpose.

To conclude, in order to find an analytic expression for general GSBs, we will need drastically different techniques.

OUR APPROACH To overcome the aforementioned challenges, in **??**, we will first develop a principled framework for analyzing the closed-form expressions of $\sigma\mathbb{W}_t$-GSBs, i.e., (6.4). Unlike the ad hoc approach of **?** which is very specific to Brownian motions, our analysis reveals the general role played by the *Lyapunov operator* (see (6.14)) on covariance matrices, thereby essentially reducing the solutions of GSBs to solving a matrix equation. This route is enabled via yet another equivalent formulation of (6.4), namely the action minimization problem on the *Bures-Wasserstein geometry*, which has

recently emerged as a rich source for inspiring new computational methods (**???**). In **??**, we show how the insight gained from our geometric framework in **??** can be easily adapted to GSBs with general reference processes, which ultimately leads to the full resolution of (GSB).

6.3 THE BURES-WASSERSTEIN GEOMETRY OF $\sigma\mathbb{W}_t$-GAUSSIAN SCHRÖDINGER BRIDGES

This section illustrates the simple geometric intuition that underlies the somewhat technical proof of our main result (cf. theorem 3). After briefly reviewing the action minimization problems on Euclidean spaces in section 6.3.1, we present the main observation in section 6.3.2: $\sigma\mathbb{W}_t$-GSBs are but action minimization problems on the Bures-Wasserstein manifolds, which can be tackled by following a standard routine in physics.

6.3.1 *A Brief Review on Action Minimization Problems*

Consider the following *action minimization* problem with fixed endpoints $x, x' \in \mathbb{R}^d$:

$$\min_{x(0)=x, x(1)=x'} \int_0^1 \frac{1}{2}\|\dot{x}(t)\|^2 - U(x(t))\,\mathrm{d}t, \tag{6.11}$$

where the minimum is taken over all piecewise smooth curves. A celebrated result in physics asserts that the optimal curve for (6.11) satisfies the *Euler-Lagrange* equation:

$$\ddot{x}(t) = -\nabla U(x(t)), \quad x(0) = x, \quad x(1) = x'. \tag{6.12}$$

In particular, when $U \equiv 0$, (6.12) reduces to $\ddot{x} \equiv 0$, i.e., $x(t)$ is a straight line connecting x and x'.

More generally, one can consider (6.11) on any *Riemannian manifold*, provided that the Euclidean norm $\|\cdot\|$ in (6.11) is replaced by the corresponding Riemannian norm. In this case, the Euler-Lagrange equation (6.12) still holds, with $\ddot{x}$ and ∇U replaced with their Riemannian counterparts (Villani, 2009).

6.3.2 *$\sigma\mathbb{W}_t$-GSBs as Action Minimization Problems*

We begin with the following simple observation. Based on the seminal work by **?**, **?** show that SBs between two arbitrary measures can be formally

understood as an action minimization problem of the form (6.11) on an *infinite*-dimensional manifold. Since we have restricted the measures in (GSB) to be Gaussian, and since Gaussian measures are uniquely determined by their means and covariances, **?** strongly suggests a *finite*-dimensional geometric interpretation of $\sigma\mathbb{W}_t$-GSBs. The main result in this section, theorem 2 below, makes this link precise.

The proper geometry we need is the *Bures-Wasserstein manifold* (**??**) defined as follows. Consider the space of covariance matrices (i.e., symmetric positive definite matrices) of dimension d, which we denote by $\mathbb{S}^d_{++}$, and consider its natural tangent space as the space of symmetric matrices:

$$\mathcal{T}_\Sigma \mathbb{S}^d_{++} := \{U \in \mathbb{R}^{d\times d} : U^\top = U\}. \tag{6.13}$$

A notion that will play a pivotal role is the so-called *Lyapunov operator*: For any $\Sigma \in \mathbb{S}^d_{++}$ and $U \in \mathcal{T}_\Sigma \mathbb{S}^d_{++}$, we define $\mathcal{L}_\Sigma[U]$ to be the symmetric solution to the equation

$$A: \quad \Sigma A + A\Sigma = U. \tag{6.14}$$

It is shown in **?** that the Lyapunov operator defines a geometry on $\mathbb{S}^d_{++}$, known as the *Bures-Wasserstein geometry*: For any two tangent vectors $U, V \in \mathcal{T}_\Sigma \mathbb{S}^d_{++}$, the operation

$$\langle U, V\rangle_\Sigma := \frac{1}{2} \operatorname{tr} \mathcal{L}_\Sigma[U] V \tag{6.15}$$

satisfies all the axioms of the Riemannian metric; additional background on the Bures-Wasserstein geometry can be found in **??**.

We are now ready to state the main result of the section. Let $\|\cdot\|_\Sigma$ be the induced norm of $\langle\cdot,\cdot\rangle_\Sigma$. Fix $\sigma > 0$ and let $\mathbb{W}_t$ be a reversible Brownian motion. Consider the following special case of (GSB):

$$\min_{\mathbb{P}_0=\mathcal{N}(0,\Sigma),\, \mathbb{P}_1=\mathcal{N}(0,\Sigma')} D_{\mathrm{KL}} \mathbb{P}_t \sigma\mathbb{W}_t. \tag{6.16}$$

Then we have:

Theorem 2 *The minimizer of* (6.16) *(and hence* (6.4)*) coincides with the solution of the action minimization problem:*

$$\min_{[0]=\Sigma,\Sigma_1=\Sigma'} \int_0^1 \frac{1}{2} \|\dot\Sigma_t\|^2 - \mathcal{U}() \, \mathrm{d}t \tag{6.17}$$

where $\mathcal{U}() := -\frac{\sigma^4}{8}\operatorname{tr}\Sigma_t^{-1}$ *and the minimum is taken over all piecewise smooth curves in* $\mathbb{S}^d_{++}$*. In particular, the minimizer of* (6.16) *solves the Euler-Lagrange equation in the Bures-Wasserstein geometry:*

$$\nabla_{\dot{\Sigma}_t}\dot{\Sigma}_t = -\operatorname{grad}\mathcal{U}(), \quad [0] = \Sigma, \quad [1] = \Sigma', \tag{6.18}$$

where $\nabla_{\dot{\Sigma}_t}\dot{\Sigma}_t$ *denotes the Riemannian acceleration and* grad *the Riemannian gradient in the Bures-Wasserstein sense.*

AN IMPORTANT IMPLICATION As alluded to in **??**, the solution curve to (6.4) or (6.16) is not new; it is derived in **?** via a strenuous and rather unenlightening calculation:

$$\Sigma_t := \bar{t}^2\Sigma + t^2\Sigma' + t\cdot\bar{t}\Big(C_\sigma + C_\sigma^\top + \sigma^2 I\Big). \tag{6.19}$$

Here, $\bar{t} := 1 - t$ and C_σ is defined in (6.2). However, the interpretation of (6.19) as the minimizer of (6.17) is new and suggests a principled avenue towards the closed-form solution of $\sigma\mathbb{W}_t$-GSBs: solve the Euler-Lagrange equation (6.18). Inspecting the formulas for $\nabla_{\dot{\Sigma}_t}\dot{\Sigma}_t$ and $\operatorname{grad}\mathcal{U}()$ (see (**??**) and (**??**)), one can further reduce (6.18) to computing the Lyapunov operator $\mathcal{L}_{\Sigma_t}[\dot{\Sigma}_t]$, which presents the bottleneck in the proof of theorem 2 as there is, in general, no closed form for the matrix equation (6.14). To this end, our main contribution is the following technical Lemma:

Lemma 1 *Define the matrix* $\tilde{S}_t$ *to be:*

$$\tilde{S}_t := t\Sigma' + \bar{t}C_\sigma - \bar{t}\Sigma - tC_\sigma^\top + \frac{\sigma^2}{2}(\bar{t} - t)I. \tag{6.20}$$

Then $\tilde{S}_t^\top\Sigma_t^{-1}$ *is symmetric.*

Armed with lemma 1, it is straightforward to verify that $\mathcal{L}_{\Sigma_t}[\dot{\Sigma}_t] = \tilde{S}_t^\top\Sigma_t^{-1}$, i.e., $\tilde{S}_t^\top\Sigma_t^{-1}$ is symmetric and satisfies:

$$\tilde{S}_t^\top\Sigma_t^{-1}\cdot\Sigma_t^{-1} + \Sigma_t^{-1}\cdot\Sigma_t^{-1}\tilde{S}_t = \tilde{S}_t^\top + \tilde{S}_t = \dot{\Sigma}_t \tag{6.21}$$

which is more or less equivalent to the original Euler-Lagrange equation (6.18); we defer the details to **??**.

To conclude, in contrast to the purely technical approach of **?**, our theorem 2 provides a geometric and conceptually clean solution for $\sigma\mathbb{W}_t$-GSBs: Compute the Lyapunov operator $\mathcal{L}_{\Sigma_t}[\dot{\Sigma}_t]$ via verifying the symmetry of the matrix in lemma 1. *It turns out that this technique can be readily extended to general GSBs*, and therefore serves as the foundation for the proof of our main result; see **??**.

REMARK It is interesting to note that the matrix $\tilde{S}_t$ in (6.20) is itself *not* symmetric. Other consequences of theorem 2 that might be of independent interest can be found in **??**. We also note that, when $\sigma = 0$, the solution to (6.17) is simply the Wasserstein geodesic between Gaussian measures, whose formula is well-known (Dowson and Landau, 1982; **?**). However, as explained in **??**, the case of $\sigma > 0$ requires a completely different analysis since, unlike when $\sigma = 0$, it is not reducible to a convex program. This leads to the significantly more involved proofs of theorem 2 and of (6.19) in **?**.

6.4 CLOSED-FORM SOLUTIONS OF GENERAL GAUSSIAN SCHRÖDINGER BRIDGES

We now present the closed-form solutions of general GSBs.

6.4.1 *Linear Stochastic Differential Equations*

We need the following background knowledge on the linear SDE Y_t. Let $\tau_t := \exp\left(\int_0^t c_s \, \mathrm{d}s\right)$. Then the solution to (6.7) is (**?**):

$$Y_t = \tau_t \left(Y_0 + \int_0^t \tau_s^{-1} \alpha_s \, \mathrm{d}s + \int_0^t \tau_s^{-1} g_s \, \mathrm{d}\mathbb{W}_s \right). \tag{6.22}$$

Another crucial fact in our analysis is that Y_t is a *Gaussian process given* Y_0, and is thus characterized by the first two moments. Using the independent increments of $\mathbb{W}_t$ and Itô's isometry (**?**), we compute:

$$\mathbb{E}[Y_t \,|\, Y_0] = \tau_t \left(Y_0 + \int_0^t \tau_s^{-1} \alpha_s \, \mathrm{d}s \right) =: \eta(t) \tag{6.23}$$

and, for any $t' \geq t$,

$$\begin{aligned} &\mathbb{E}\left[(Y_t - \eta(t)) \left(Y_{t'} - \eta(t')\right)^\top \,\middle|\, Y_0 \right] \\ &\qquad = \left(\tau_t \tau_{t'} \int_0^t \tau_s^{-2} g_s^2 \, \mathrm{d}s \right) I =: \kappa(t, t') I. \end{aligned} \tag{6.24}$$

6.4.2 *Main Result*

We now present the main result of our paper. With the important application of diffusion-based models in mind, we will not only derive solution curves as in (6.19) but also their SDE representations.

SDE with $\alpha_t \equiv 0$	Setting	$\kappa(t,t')$	$\sigma_\star^2$	r_t	$\bar{r}_t$	ρ_t	$\zeta(t)$
BM	$c_t \equiv 0$ $g_t \equiv \omega \in \mathbb{R}^+$	$\omega^2 t$	ω^2	t	$1-t$	t	0
VESDE	$c_t \equiv 0$ $g_t = \sqrt{\dot{q}(t)}$	$q(t)$	$q(1)$	$\frac{q(t)}{q(1)}$	$1-\frac{q(t)}{q(1)}$	$\frac{q(t)}{q(1)}$	0
VPSDE	$-2c_t = g_t^2$	$\tau_{t'}\left(\tau_t^{-1}-\tau_t\right)$	$\tau_1^{-1}-\tau_1$	$\frac{\tau_t^{-1}-\tau_t}{\tau_1^{-1}-\tau_1}$	$\tau_1\left(\frac{\tau_t}{\tau_1}-\frac{\tau_t^{-1}-\tau_t}{\tau_1^{-1}-\tau_1}\right)$	$\frac{\tau_t^{-1}\left(\tau_t^{-1}-\tau_t\right)}{\tau_1^{-1}\left(\tau_1^{-1}-\tau_1\right)}$	0
sub–VPSDE	$\frac{g_t^2}{-2c_t} = 1-\tau_t^4$	$\tau_t\tau_{t'}\left(\tau_t^{-1}-\tau_t\right)^2$	$\tau_1\left(\tau_1^{-1}-\tau_1\right)^2$	$\frac{\tau_t}{\tau_1}\cdot\left(\frac{\tau_t^{-1}-\tau_t}{\tau_1^{-1}-\tau_1}\right)^2$	$\tau_t\left(1-\left(\frac{\tau_t^{-1}-\tau_t}{\tau_1^{-1}-\tau_1}\right)^2\right)$	$\left(\frac{\tau_t^{-1}-\tau_t}{\tau_1^{-1}-\tau_1}\right)^2$	0
SDE with $\alpha_t \not\equiv 0$	**Setting**	$\kappa(t,t')$	$\sigma_\star^2$	r_t	$\bar{r}_t$	ρ_t	$\zeta(t)$
OU/Vasicek	$c_t \equiv -\lambda \in \mathbb{R}$ $\alpha_t \equiv \mathbf{v} \in \mathbb{R}^d$ $g_t \equiv \omega \in \mathbb{R}^+$	$\frac{\omega^2 e^{-\lambda t'}\sinh\lambda t}{\lambda}$	$\frac{\omega^2\sinh\lambda}{\lambda}$	$\frac{\sinh\lambda t}{\sinh\lambda}$	$\sinh\lambda t\coth\lambda t$ $-\sinh\lambda t\coth\lambda$	$e^{-\lambda(1-t)}$ $\cdot\frac{\sinh\lambda t}{\sinh\lambda}$	$\frac{\mathbf{v}}{\lambda}\left(1-e^{-\lambda t}\right)$
α_t-BDT	$c_t \equiv 0$ $g_t \equiv \omega \in \mathbb{R}^+$	$\omega^2 t$	$\omega^2 1$	t	$1-t$	t	$\int_0^t \alpha_s \, \mathrm{d}s$

Table 6.1: Examples of reference SDEs and the corresponding solutions of GSBs. All relevant functions in the Table are either introduced in section 6.4.1 or (6.25).

Let $\xi = \mathcal{N}(\mu_0, \Sigma_0)$ and $\xi' = \mathcal{N}(\mu_1, \Sigma_1)$ be two arbitrary Gaussian distributions in (GSB), and let D_σ, C_σ be as defined in (6.2).

Theorem 3 *Denote by $\mathbb{P}_t$ the solution to Gaussian Schrödinger bridges (GSB). Set*

$$
\begin{aligned}
&r_t := \frac{\kappa(t,1)}{\kappa(1,1)}, \quad \bar{r}_t := \tau_t - r_t\tau_1, \quad \sigma_\star := \sqrt{\tau_1^{-1}\kappa(1,1)}, \\
&\zeta(t) := \tau_t \int_0^t \tau_s^{-1}\alpha_s \, \mathrm{d}s, \rho_t := \frac{\int_0^t \tau_s^{-2} g_s^2 \, \mathrm{d}s}{\int_0^1 \tau_s^{-2} g_s^2 \, \mathrm{d}s}, \\
&P_t := \dot{r}_t(r_t\Sigma_1 + \bar{r}_t C_{\sigma_\star}), \quad Q_t := -\dot{\bar{r}}_t(\bar{r}_t\Sigma_0 + r_t C_{\sigma_\star}), \\
&S_t := P_t - Q_t^\top + \left[c_t\kappa(t,t)(1-\rho_t) - g_t^2\rho_t\right] I.
\end{aligned} \tag{6.25}
$$

Then the following holds:

1. *The solution $\mathbb{P}_t$ is a Markov Gaussian process whose marginal variable $X_t \sim \mathcal{N}(\mu_t, \Sigma_t)$, where*

$$
\mu_t := \bar{r}_t\mu_0 + r_t\mu_1 + \zeta(t) - r_t\zeta(1), \tag{6.26}
$$

$$
\Sigma_t := \bar{r}_t^2\Sigma_0 + r_t^2\Sigma_1 + r_t\bar{r}_t\left(C_{\sigma_\star} + C_{\sigma_\star}^\top\right) + \kappa(t,t)(1-\rho_t)I. \tag{6.27}
$$

2. *X_t admits a closed-form representation as the SDE:*

$$
\mathrm{d}X_t = f_{\mathcal{N}}(t, X_t)\,\mathrm{d}t + g_t\,\mathrm{d}W_t \tag{6.28}
$$

where

$$f_{\mathcal{N}}(t,x) := S_t^\top \Sigma_t^{-1}(x-\mu_t) + \dot{\mu}_t. \tag{6.29}$$

Moreover, the matrix $S_t^\top \Sigma_t^{-1}$ is symmetric.

As in theorem 2, the key step in the proof of theorem 3 is to recognize the symmetry of the matrix $S_t^\top \Sigma_t^{-1}$ where S_t, defined in (6.25), simply becomes the $\tilde{S}_t$ in lemma 1 (up to an additive factor of $\frac{\sigma^2 \bar{t}}{2} I$) for $\sigma \mathbb{W}_t$-GSBs. Although this can be directly verified via generalizing lemma 1, the computation becomes quite tedious, so our proof of theorem 3 will follow a slightly different route. In any case, given the symmetry of $S_t^\top \Sigma_t^{-1}$, the proof simply boils down to a series of straightforward calculations; see **??**.

CLOSED FORMS FOR CONDITIONAL DISTRIBUTIONS In many practical applications such as generative modeling, a requirement to employ the SDE representation of GSBs in (6.28) is that its *conditional distributions* given the initial points can be computed efficiently. As an immediate corollary of theorem 3, we obtain the following closed-form expressions for these conditional distributions.

Corollary 1 *Let $X_t \sim \mathbb{P}_t$ be the the solution to (GSB). Then the conditional distribution of X_t given end points has a simple solution: $X_t | X_0 = x_0 \sim \mathcal{N}\left(\mu_{t|0}, \Sigma_{t|0}\right)$, where*

$$\mu_{t|0} = \bar{r}_t x_0 + r_t\left(\mu_1 + C_{\sigma_\star}^\top \Sigma_0^{-1}(x_0 - \mu_0)\right) + \zeta(t) - r_t \zeta(1), \tag{6.30}$$

$$\Sigma_{t|0} = r_t^2\left(\Sigma_1 - C_\sigma^\top \Sigma_0^{-1} C_\sigma\right) + \kappa(t,t)(1-\rho_t) I. \tag{6.31}$$

Similarly, $X_t | X_1 = x_1 \sim \mathcal{N}\left(\mu_{t|1}, \Sigma_{t|1}\right)$, where

$$\mu_{t|1} = r_t x_1 + \bar{r}_t\left(\mu_0 + C_{\sigma_\star} \Sigma_1^{-1}(x_1 - \mu_1)\right) + \zeta(t) - r_t \zeta(1), \tag{6.32}$$

$$\Sigma_{t|1} = \bar{r}_t^2\left(\Sigma_0 - C_\sigma \Sigma_1^{-1} C_\sigma^\top\right) + \kappa(t,t)(1-\rho_t) I. \tag{6.33}$$

Examples of GSBs. Our framework captures most popular reference SDEs in the machine learning literature as well as other mathematical models in financial engineering; see table 6.1. A non-exhaustive list includes:

- The basic Brownian motion (BM) and the Ornstein-Uhlenbeck (OU) processes, both widely adopted as the reference process for SB-based models (**?**De Bortoli et al., 2021; Lavenant et al., 2021; Vargas et al., 2021;

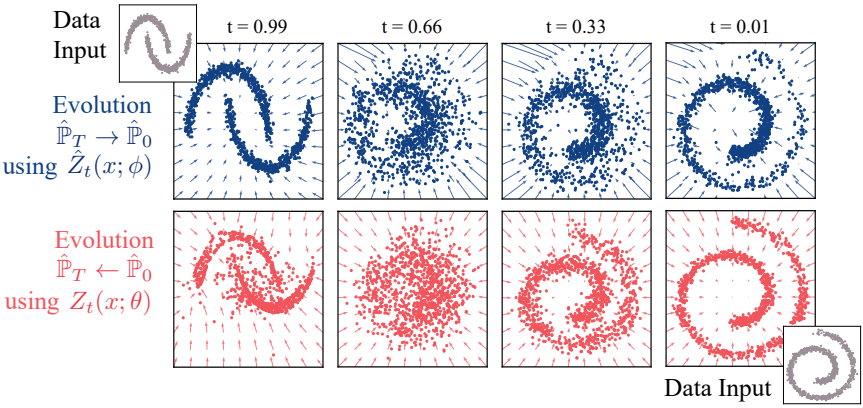

FIGURE 6.2: Illustration of the time-dependent drifts learned by GSBFLOW with VE SDE for two toy marginal distributions. *Top.* Evolution of $\hat{\mathbb{P}}_1$ (moons) $\to \hat{\mathbb{P}}_0$ (spiral) via backward policy $\hat{Z}_t^{\phi}(x)$. *Bottom.* Evolution of $\hat{\mathbb{P}}_0$ (spiral) $\to \hat{\mathbb{P}}_1$ (moons) via forward policy $Z_t^{\theta}(x)$.

?). We also remark that, even though (6.27) is known for BM (**?**), what is crucial in these applications is the SDE presentation (6.28), which is new even for BM.

- The variance exploding SDEs (VESDEs), which underlies the training of score matching with Langevin dynamics for diffusion-based generative modeling (**??**Song et al., 2021).
- The variance preserving SDEs (VPSDEs), which can be seen as the continuous limit of denoising diffusion probabilistic models (**??**Song et al., 2021), another important class of algorithms for diffusion-based generative modeling.
- The *sub-VPSDEs* proposed by (Song et al., 2021), which are motivated by reducing the variance of VPSDEs.
- Several important SDEs in financial engineering, such as the *Vasicek model* (which generalizes OU processes) and the *constant volatility* α_t*-Black-Derman-Toy (BDT) model* (**?**).

Method	Tasks	
	Wasserstein Loss $W_\varepsilon \downarrow$	
	?	Schiebinger et al. (2019b)
Song et al. (2021)		
VESDE	20.83 ± 0.18	40.81 ± 0.42
sub-VPSDE	$\mathbf{19.96 \pm 0.58}$	48.15 ± 3.38
GSBFLOW (*ours*)		
VESDE	25.18 ± 0.10	$\mathbf{27.85 \pm 0.68}$

TABLE 6.2: Evaluation of predictive performance w.r.t. the entropy-regularized Wasserstein distance W_ε (Cuturi, 2013) of GSBFLOW and baselines on generating different single-cell datasets (using 3 runs).

6.5 EMPIRICAL EVALUATION

The purpose of our experiments is to demonstrate that, by leveraging moment information, GSBFLOW is significantly more stable compared to other SB-based objectives, especially when moving beyond the *generative* setting where $\hat{\mathbb{P}}_1$ is a simple Gaussian. Indeed, while performing competitively in the generative setting ($\mathcal{N}_0 \to \hat{\mathbb{P}}_1$), our method *outperforms* when modeling the evolution of two complex distributions ($\hat{\mathbb{P}}_0 \to \hat{\mathbb{P}}_1$), the most general and ambitious setting to estimate a bridge. This is demonstrated on synthetic data as well as a task from molecular biology concerned with modeling the dynamics of cellular systems, i.e., single-cell genomics (**?**Frangieh et al., 2021; **?**).

6.5.1 *Synthetic Dynamics*

Before conducting the single-cell genomics experiments, we first test GSBFLOW on a synthetic setting. Our first task involves recovering the stochastic evolution of two-dimensional synthetic data containing two interleaving half circles ($\hat{\mathbb{P}}_1$) into a spiral ($\hat{\mathbb{P}}_0$). fig. 6.2 shows the trajectories learned by GSBFLOW based on the VESDE (see table 6.1 and **??**).

While it is sufficient to parameterize only a single policy ($\hat{Z}_t^\phi(x)$) in generative modeling, the task of learning to evolve $\hat{\mathbb{P}}_0$ into $\hat{\mathbb{P}}_1$ requires one to recover *both* vector fields $\hat{Z}_t^\phi(x)$ and $Z_t^\theta(x)$. As demonstrated in

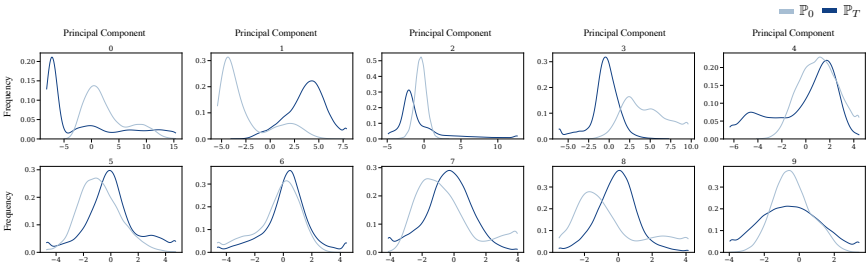

FIGURE 6.3: The expression levels of the first 10 principal components from the dataset by Schiebinger et al. (2019b).

fig. 6.2, GSBFLOW is able to successfully learn both policies $Z_t^\theta(x)$ and $\hat{Z}_t^\phi(x)$ and reliably recovers the corresponding targets of the forward and backward evolution. While initializing the reference process through the closed-form SB between the Gaussian approximations of both synthetic datasets provides good results, the power of GSBFLOW becomes evident in more complex applications which we tackle next.

6.5.2 *Single-Cell Dynamics*

Modern single-cell profiling technologies are able to provide rich feature representations (e.g., gene expression) of *individual* cells at any development state. A crucial issue that arises with such profiling methods is their destructive nature: Measuring a cell requires destroying it and thus a cell cannot be measured twice. As a result, independent samples are collected at each snapshot, with no access to ground-truth single-cell trajectories throughout time, resulting in challenging, *unaligned*, datasets. Recovering cellular dynamics from such unaligned snapshots, i.e., $\hat{\mathbb{P}}_0$ to $\hat{\mathbb{P}}_1$, has, however, extremely important scientific and biomedical relevance (**?**). For example, it determines our understanding on how and why tumor cells evade cancer therapies (Frangieh et al., 2021) or unveils mechanisms of cell differentiation and development (Schiebinger et al., 2019b). Following related work, in particular previous methods based on optimal transport (Schiebinger et al., 2019b; Bunne et al., 2021, 2022a; Tong et al., 2020), the task is thus to learn the stochastic process that described the evolution of single cells from $\hat{\mathbb{P}}_0$ to $\hat{\mathbb{P}}_1$.

6.5.2.1 *Experimental Setup*

SINGLE-CELL GENOMICS VIA Let us consider the evolution of a gene, for which we can collect the empirical distributions $\hat{\mathbb{P}}_0, \hat{\mathbb{P}}_1$ of its expression levels at the times $t = 0, 1$ (Schiebinger et al., 2019b; **?**). Our goal is to two-fold:

1. To solve the **generative modeling** problem, i.e., to generate $\hat{\mathbb{P}}_0$ or $\hat{\mathbb{P}}_1$ from a standard Gaussian noise, and
2. to **evolve** $\mathbb{P}_0 \to \mathbb{P}_1$ or $\mathbb{P}_1 \to \mathbb{P}_0$, i.e., to recover a stochastic process $\mathbb{P}_t$ satisfying $\mathbb{P}_0 = \hat{\mathbb{P}}_0, \mathbb{P}_1 = \hat{\mathbb{P}}_1$.

Although there are numerous algorithms for generative modeling, to our knowledge, the only framework that can simultaneously solve both tasks is the SB-based scheme recently proposed in (Chen et al., 2022a). In order to apply this framework, one has to choose a prior process Y_t, which is taken by the authors to be the high-performing VESDE and sub-VPSDE. These SB-based methods, as well as several standard generative modeling algorithms (**??**Song et al., 2021; **?**; **?**,**?**) for the first task, constitute strong baselines for our experiments.

OUR CHOICE OF Y_t; THE GSBFLOW Instead of directly diving into the numerical solution of SBs as in Chen et al. (2022a), we first empirically verify that the distributions $\hat{\mathbb{P}}_0, \hat{\mathbb{P}}_1$ in single-cell genomics are typically close to *non-standard* Gaussian distributions: See fig. 6.3 for the canonical dataset (Schiebinger et al., 2019b) and **??** in **??** for the same phenomenon on another standard benchmark (**?**).

Since the solutions of SBs are Lipschitz in terms of $\hat{\mathbb{P}}_0, \hat{\mathbb{P}}_1$ (**?**), a reasonable approximation to the original SB objective is to replace $\hat{\mathbb{P}}_0, \hat{\mathbb{P}}_1$ by Gaussians with matching moments. This results in a GSB problem which can be solved in closed form by our theorem 3. Intuitively, if we denote an existing prior process by Y_t and the solution of its corresponding GSB by X_t, then X_t presents a more appealing prior process than Y_t since it carries the moment information of $\hat{\mathbb{P}}_0$ and $\hat{\mathbb{P}}_1$, whereas Y_t is completely data-oblivious.

Motivated by these observations, we propose a simple modification of the framework in Chen et al. (2022a): Replace the prior process Y_t by its GSB approximation and keep everything else the same. The resulting scheme, which we term the GSBFLOW, learns a pair of forward $Z_t^\theta(x)$ and backward parametrized drifts $\hat{Z}_t^\phi(x)$ that progressively transport samples from $\hat{\mathbb{P}}_0 \to \hat{\mathbb{P}}_1$ and $\hat{\mathbb{P}}_1 \to \hat{\mathbb{P}}_0$, respectively. The full algorithm is presented in **??** for completeness.

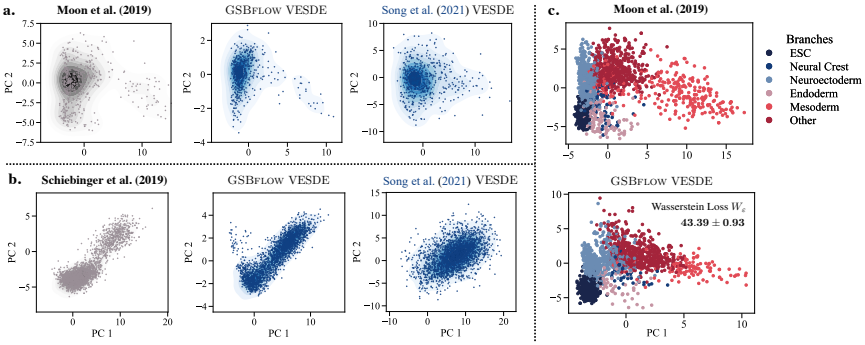

FIGURE 6.4: **a.-b.** Visual evaluation of the ability of our method to model the **generation** of data from **a. ?** and **b.** Schiebinger et al. (2019b). Density plots are visualized in 2D PCA space and show generated data points using either GSBFLOW (our method) or the procedure in Song et al. (2021). **c.** Evaluation of GSBFLOW's ability to model the entire **evolution** of a developmental process of **?**, visualized by the data and GSBFLOW predictions colored by the lineage branch class.

6.5.2.2 *Results*

We investigate the ability of GSBFLOW to generate cell populations $\hat{\mathbb{P}}_1$ from noise $\mathcal{N}_0$ ($\mathcal{N}_0 \to \hat{\mathbb{P}}_1$, Fig. 6.4a, b) on the the canonical datasets (**?**Schiebinger et al., 2019b); as well as to predict the dynamics of single-cell genomics ($\hat{\mathbb{P}}_0 \to \hat{\mathbb{P}}_1$, Fig. 6.4c) (**?**), i.e., the inference of cell populations $\hat{\mathbb{P}}_1$ resulting from the developmental process of an initial cell population $\hat{\mathbb{P}}_0$, with the goal of learning individual dynamics, identify ancestor and descendant cells. Details on datasets and experimental design can be found in **??**–**??**. The evaluation is conducted on the first 20 or 30 components of the PCA space of the > 1500 highly differentiable genes (see **??**–**??**).

We evaluate the quality of the generated cellular states through the entropy-regularized Wasserstein distance W_ε (see table 6.2) and by visualizing the first two principal components (PC), see fig. 6.4a, b. GSBFLOW performs competitively on reconstructing embryoid body differentiation landscapes (**?**), and outperforms score-based generative models baselines on the iPSC reprogramming task (Schiebinger et al., 2019b) as quantified by W_ε between data and predictions. Further, we analyze GSBFLOW's ability to predict the temporal evolution of embryoid body differentiation (**?**), where cells measured at day 1 to 3 serve as samples of $\hat{\mathbb{P}}_0$, while $\hat{\mathbb{P}}_1$ is constructed

from samples between day 12 to 27. As no ground truth trajectories are available in the data, we compare the predicted evolution to the data and compare how well the heterogeneity of lineage (fig. 6.4c, upper panel) or sublineage branches (**??**a) is captured. fig. 6.4c (lower panel) and **??**b thereby closely resemble the data (see W_ε in fig. 6.4c) and thus demonstrate GSBFLOW's ability to learn cell differentiation into various lineages and to capture biological heterogeneity on a more macroscopic level.

6.6 CONCLUSION

We derive closed-form solutions of GSBs, an important class of dynamic OT problems. Our technique originates from a deep connection between Gaussian OT and the Bures-Wasserstein geometry, which we generalize to the case of general SB problems. Numerically, we demonstrate that our new closed forms inspire a simple modification of existing SB-based numerical schemes, which can however lead to significantly improved performance.

Limitation of our framework. In a broader context, we hope our results can serve as the inspiration for more learning algorithms, much like how existing closed-form solutions of Gaussian OT problems have contributed to the machine learning community. We thus acknowledge a severe limitation of our closed-form solutions: These formulas require matrix inversions, which might face scalability issues for high-dimensional data. In addition, existing matrix inversion algorithms are typically extremely sensitive to the condition number, and thus our formulas are not as useful for ill-conditioned data. Lifting these constraints to facilitate further applications, such as to image datasets, is an important future work.

7

...

...

— ..., ... (...)

Interpolation, the task of transforming one given distribution into another, lies at the heart of many modern machine learning applications such as single-cell genomics (Tong et al., 2020; Schiebinger et al., 2019b; Bunne et al., 2022a), meteorology (Fisher et al., 2009), and robotics (Chen et al., 2021a). To this end, DSB (De Bortoli et al., 2021; Chen et al., 2022a; Vargas et al., 2021; Liu et al., 2022) have recently emerged as a powerful paradigm due to their ability to generalize prior deep diffusion-based models, notably SMLD (**?**Song et al., 2021) and DDPM (**?**), which have achieved the state-of-the-art on many generative modeling problems.

Despite the wide success, a significant limitation of existing frameworks for solving DSB is that they fail to capture the *alignment* of data: If $\hat{\mathbb{P}}_0, \hat{\mathbb{P}}_1$ are two (empirical) distributions between which we wish to interpolate, then a tacit assumption in the literature is that the dependence of $\hat{\mathbb{P}}_0$ and $\hat{\mathbb{P}}_1$ is unknown and somehow has to be recovered. Such an assumption, however, ignores important scenarios where the data is *aligned*, meaning that the samples from $\hat{\mathbb{P}}_0$ and $\hat{\mathbb{P}}_1$ naturally come in pairs $(\mathbf{x}_0^i, \mathbf{x}_1^i)_i^N$, which is common in many biological phenomena. Proteins, for instance, undergo conformational changes upon interactions with other biomolecules (protein docking, see Fig. 7.1). The goal is to model conformational changes by recovering a (stochastic) trajectory $\mathbf{x}_t$ based on the positions observed at two-time points $(\mathbf{x}_0, \mathbf{x}_1)$. Failing to incorporate this alignment would mean that we completely ignore information on the correspondence between the initial and final points of the molecules, resulting in a much harder problem than necessary. Beyond, the recent use of SBs has been motivated by an important task in molecular biology: Cells change their molecular profile throughout developmental processes (Schiebinger et al., 2019b; **?**) or in response to perturbations such as cancer drugs (Lotfollahi et al., 2019; Bunne et al., 2021). As most measurement technologies are destructive assays, i.e., the same cell cannot be observed twice nor fully profiled over time, these methods aim at reconstructing cell dynamics from *unpaired* snapshots. Recent developments in molecular biology, however, aim at overcoming this technological limitation. For example, Chen et al. (2022b) propose a

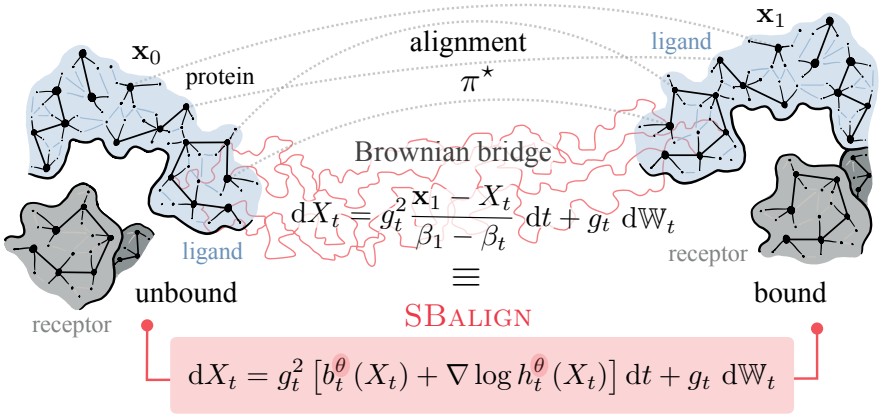

FIGURE 7.1: Overview of SBALIGN: In biological tasks such as protein docking, one is naturally provided with *aligned* data in the form of unbound and bound structures of participating proteins. Our goal is to therefore recover a stochastic trajectory from $\mathbf{x}_0$ to $\mathbf{x}_1$. To achieve this, we connect the characterization of an SDE conditioned on $\mathbf{x}_0$ and $\mathbf{x}_1$ (utilizing the Doob's *h-transform*) with that of a Brownian bridge between $\mathbf{x}_0$ and $\mathbf{x}_1$ (classical Schrödinger bridge theory). We show that this leads to a simpler training procedure with lower variance and strong empirical results.

transcriptome profiling approach that preserves cell viability. Weinreb et al. (2020) capture cell differentiation processes by clonally connecting cells and their progenitors through barcodes (see illustrative Figure in Supplement).

Motivated by these observations, the goal of this paper is to propose a novel algorithmic framework for solving DSB with (partially) *aligned* data. Our approach is in stark contrast to existing works which, due to the lack of data alignment, all rely on some variants of IPF (**??**) and are thus prone to numerical instability. On the other hand, via a combination of the original theory of Schrödinger bridges (Schrödinger, 1931; **?**) and the key notion of Doob's *h-transform* (**??**), we design a novel loss function that completely bypasses the IPF procedure and can be trained with much lower variance.

To summarize, we make the following contributions:

- To our best knowledge, we consider, for the first time, the problem of interpolation with *aligned* data. We rigorously formulate the problem in the DSB framework.

- Based on the theory of Schrödinger bridges and h-transform, we derive a new loss function that, unlike prior work on DSB, does not require an IPF-like procedure to train. We also propose principled regularization schemes to further stabilize training.
- We describe how interpolating aligned data can provide better reference processes for use in classical DSB, paving the way to hybrid aligned/non-aligned SB.
- We evaluate our proposed framework on both synthetic and real data. For experiments utilizing real data, we consider two tasks where such aligned data is naturally available. The first is the task of developmental processes in single-cell biology, and the second is (*rigid*) protein docking, where the goal is to predict the 3D structure of the bound complex formed by two proteins, given their unbound 3D structures. Our method demonstrates a considerable improvement over prior methods across various metrics, thereby substantiating the importance of taking the data alignment into account.

RELATED WORK Solving DSB is a subject of significant interest in recent years and has flourished in a number of different algorithms (De Bortoli et al., 2021; Chen et al., 2022a; Vargas et al., 2021; Bunne et al., 2023; **?**). However, all these previous approaches focus on *unaligned* data, and therefore the methodologies all rely on IPF and are hence drastically different from ours. In the experiments, we will demonstrate the importance of taking the alignment of data into consideration by comparing our method to these baselines.

An important ingredient in our theory is Doob's h-transform, which has recently also been utilized by **?** to solve the problem of constrained diffusion. However, their fundamental motivation is different from ours. **?** focus on learning the drift of the diffusion model and the h-transform *together*, whereas ours is to read off the drift *from* the h-transform with the help of *aligned data*. Consequently, there is no overlap between the two algorithms and their intended applications.

To the best of our knowledge, the concurrent work of Tong et al. (2023) is the only existing framework that can tackle aligned data, which, however, is not their original motivation. In the context of solving DSB, their algorithm can be seen as learning a vector field that generates the correct *marginal* probability (cf. Tong et al., 2023, Proposition 4.3). Importantly, this is different from our aim of finding the *pathwise* optimal solution of DSB: If

$(\mathbf{x}^i_{0,\text{test}})_{i=1}^m$ is a test data set for which we wish to predict their destinations, then the framework of Tong et al. (2023) can only ensure that the marginal distribution $(\mathbf{x}^i_{1,\text{test}})_{i=1}^m$ is correct, whereas ours is capable of predicting that $\mathbf{x}^i_{1,\text{test}}$ is precisely the destination of $\mathbf{x}^i_{0,\text{test}}$ for each i. This latter property is highly desirable in tasks like ML-accelerated protein docking.

PROBLEM FORMULATION Suppose that we are given access to i.i.d. *aligned* data $(\mathbf{x}^i_0, \mathbf{x}^i_1)_{i=1}^N$, where the marginal distribution of $\mathbf{x}^i_0$'s is $\hat{\mathbb{P}}_0$ and of $\mathbf{x}^i_1$'s is $\hat{\mathbb{P}}_1$. Typically, we view $\hat{\mathbb{P}}_0$ as the empirical marginal distribution of a stochastic process observed at time $t = 0$, and likewise $\hat{\mathbb{P}}_1$ the empirical marginal observed at $t = 1$. The goal is to reconstruct the stochastic process $\mathbb{P}_t$ based on $(\mathbf{x}^i_0, \mathbf{x}^i_1)_{i=1}^N$, to *interpolate* between $\hat{\mathbb{P}}_0$ and $\hat{\mathbb{P}}_1$.

Such a task is ubiquitous in biological applications. For instance, understanding how proteins dock to other biomolecules is of significant interest in biology and has become a topic of intense study in recent years (**??**Corso et al., 2023). In the protein docking task, $\mathbf{x}^i_0$ represents the 3D structures of the unbound proteins, while $\mathbf{x}^i_1$ represents the 3D structure of the bound complex. Reconstructing a stochastic process that diffuses $\mathbf{x}^i_0$'s to $\mathbf{x}^i_1$'s is tantamount to recovering the energy landscape governing the docking process. Similarly, in molecular dynamics simulations, we have access to trajectories $(\mathbf{x}^i_t)_{t\in[0,1]}$, where $\mathbf{x}^i_0$ and $\mathbf{x}^i_1$ represent the initial and final positions of the i-th molecule respectively. Any learning algorithm using these simulations should be able to respect the provided alignment.

DIFFUSION SCHRÖDINGER BRIDGES To solve the interpolation problem, in **??**, we will invoke the framework of DSBs, which are designed to solve interpolation problems with *unaligned* data. More specifically, given two marginals $\hat{\mathbb{P}}_0$ and $\hat{\mathbb{P}}_1$, the DSB framework proceeds by first choosing a reference process $\mathbb{Q}_t$ using prior knowledge, for instance a simple Brownian motion, and then solve the entropy-minimization problem over all stochastic processes $\mathbb{P}_t$:

$$\min_{\mathbb{P}_0=\hat{\mathbb{P}}_0,\, \mathbb{P}_1=\hat{\mathbb{P}}_1} D_{\text{KL}}\mathbb{P}_t\mathbb{Q}_t. \tag{SB}$$

Despite the fact that many methods exist for solving (SB) (De Bortoli et al., 2021; Chen et al., 2022a; Vargas et al., 2021; Bunne et al., 2023), none of these approaches are capable of incorporating *alignment* of the data. This can be seen by inspecting the objective (SB), in which the coupling information $(\mathbf{x}^i_0, \mathbf{x}^i_1)$ is completely lost as only its individual marginals $\hat{\mathbb{P}}_0, \hat{\mathbb{P}}_1$ play a role therein. Unfortunately, it is well-known that tackling

the marginals separately necessitates a forward-backward learning process known as the iterative proportional fitting procedure (**??**), which constitutes the primary reason of high variance training, thereby confronting DSB with numerical and scalability issues. Our major contribution, detailed in the next section, is therefore to devise the first algorithmic framework that solves the interpolation problem with aligned data *without* resorting to IPF.

7.1 ALIGNED DIFFUSION SCHRÖDINGER BRIDGES

In this section, we derive a novel loss function for DSBs with aligned data by combining two classical notions: The theory of Schrödinger bridges (Schrödinger, 1931; **?**; Chen et al., 2021b) and Doob's h-transform (**??**). We then describe how solutions to DSBs with aligned data can be leveraged in the context of classical DSBs.

7.1.1 *Learning aligned diffusion Schrödinger bridges*

STATIC SB AND ALIGNED DATA Our starting point is the simple and classical observation that (SB) is the continuous-time analogue of the *entropic optimal transport*, also known as the *static* SB problem (**?**Chen et al., 2021b; Peyré and Cuturi, 2019):

$$\pi^\star := \underset{\mathbb{P}_0=\hat{\mathbb{P}}_0,\, \mathbb{P}_1=\hat{\mathbb{P}}_1}{\arg\min} \; D_{\mathrm{KL}}\mathbb{P}_{0,1}\mathbb{Q}_{0,1} \tag{7.1}$$

where the minimization is over all *couplings* of $\hat{\mathbb{P}}_0$ and $\hat{\mathbb{P}}_1$, and $\mathbb{Q}_{0,1}$ is simply the joint distribution of $\mathbb{Q}_t$ at $t = 0, 1$. In other words, if we denote by $\mathbb{P}_t$ the stochastic process that minimizes (SB), then the joint distribution $\mathbb{P}_{0,1}$ necessarily coincides with the $\pi^\star$ in (7.1). Moreover, since in DSB, the data is always assumed to arise from $\mathbb{P}_t$, we see that:

> The *aligned* data $(\mathbf{x}_0^i, \mathbf{x}_1^i)_{i=1}^N$ constitutes samples of $\pi^\star$.

This simple but crucial observation lies at the heart of all derivations to come.

Our central idea is to represent $\mathbb{P}_t$ via two different, but equivalent, characterizations, both of which involve $\pi^\star$: That of a *mixture* of reference processes with pinned end points, and that of conditional SDE.

$\mathbb{P}_t$ FROM $\pi^\star$: $\mathbb{Q}_t$ WITH PINNED END POINTS For illustration purposes, from now on, we will assume that the reference process $\mathbb{Q}_t$ is a Brownian motion with diffusion coefficient g_t:

$$\mathrm{d}\mathbb{Q}_t = g_t \, \mathrm{d}\mathbb{W}_s. \tag{7.2}$$

In this case, it is well-known that $\mathbb{Q}_t$ *conditioned* to start at $\mathbf{x}_0$ and end at $\mathbf{x}_1$ can be written in another SDE (**??**):

$$\mathrm{d}X_t = g_t^2 \frac{\mathbf{x}_1 - X_t}{\beta_1 - \beta_t} \, \mathrm{d}t + g_t \, \mathrm{d}\mathbb{W}_s \tag{7.3}$$

where $X_0 = \mathbf{x}_0$ and

$$\beta_t \coloneqq \int_0^t g_s^2 \, \mathrm{d}s. \tag{7.4}$$

We call the processes in (7.3) the *scaled Brownian bridges* as they generalize the classical Brownian bridge, which corresponds to the case of $g_t \equiv 1$.

The first characterization of $\mathbb{P}_t$ is then an immediate consequence the following classical result in SB theory: Draw a sample $(\mathbf{x}_0, \mathbf{x}_1) \sim \pi^\star$ and connect them via (7.3). The resulting path is a sample from $\mathbb{P}_t$ (**?**Chen et al., 2021b). In other words, $\mathbb{P}_t$ is a *mixture* of scaled Brownian bridges, with the mixing weight given by $\pi^\star$.

$\mathbb{P}_t$ FROM $\pi^\star$: REPRESENTATION Another characterization of $\mathbb{P}_t$ is that it is itself given by an SDE of the form (**?**Chen et al., 2021b)

$$\mathrm{d}X_t = g_t^2 b_t(X_t) \, \mathrm{d}t + g_t \, \mathrm{d}\mathbb{W}_s. \tag{7.5}$$

Here, $b_t : \mathbb{R}^d \to \mathbb{R}^d$ is a time-dependent drift function that we wish to learn.

Now, by Doob's h-transform, we know that the SDE (7.5) *conditioned* to start at $\mathbf{x}_0$ and end at $\mathbf{x}_1$ is given by another SDE (**??**):

$$\mathrm{d}X_t = g_t^2 [b_t(X_t) + \nabla \log h_t(X_t)] \, \mathrm{d}t + g_t \, \mathrm{d}\mathbb{W}_s \tag{7.6}$$

where $h_t(\mathbf{x}) \coloneqq \mathbb{P}(X_1 = \mathbf{x}_1 | X_t = \mathbf{x})$ is the *Doob's h function*. Notice that we have suppressed the dependence of h_t on $\mathbf{x}_0$ and $\mathbf{x}_1$ for notational simplicity.

LOSS FUNCTION Since both (7.3) and (7.6) represent $\mathbb{P}_t$, the solution of the DSB, the two SDE must coincide. In other words, suppose we parametrize b_t as b_t^θ, then, by matching terms in (7.3) and (7.6), we can learn the optimal parameter $\theta^\star$ via optimization of the loss function

$$L(\theta) \coloneqq \mathbb{E}\left[\int_0^1 \left\| \frac{\mathbf{x}_1 - X_t}{\beta_1 - \beta_t} - \nabla \log h_t^\theta(X_t) \right\|^2 \mathrm{d}t \right] \tag{7.7}$$

Algorithm 1 SBALIGN

Input: Aligned data $(\mathbf{x}_0^i, \mathbf{x}_1^i)_{i=1}^N$, learning rates $\gamma_\theta, \gamma_\phi$, number of iterations K

Initialize $\theta \leftarrow \theta_0$, $\phi \leftarrow \phi_0$.
for $k = 1$ **to** K **do**
  Draw a mini-batch of samples from $(\mathbf{x}_0^i, \mathbf{x}_1^i)_{i=1}^N$
  Compute empirical average of (7.12) with mini-batch.
  Update $\phi \leftarrow \phi - \gamma_\phi \nabla L(\theta, \phi)$
  Update $\theta \leftarrow \theta - \gamma_\theta \nabla L(\theta, \phi)$

where h_t^θ is determined by b_t^θ as well as the drawn samples $(\mathbf{x}_0, \mathbf{x}_1)$. In short, assuming that, for each θ, we can compute h_t^θ *based only on* b_t^θ, we can then backprop through (7.7) and optimize it using any off-the-shelf algorithm.

A SLIGHTLY MODIFIED (7.7) Even with infinite data and a neural network with sufficient capacity, the loss function defined in (7.7) does converge to 0. For the purpose of numerical stability, we instead propose to modify (7.7) to:

$$L(\theta) := \mathbb{E}\left[\int_0^1 \left\| \frac{\mathbf{x}_1 - X_t}{\beta_1 - \beta_t} - \left(b_t^\theta + \nabla \log h_t^\theta(X_t)\right)\right\|^2 \mathrm{d}t\right] \tag{7.8}$$

which is clearly equivalent to (7.7) at the true solution of b_t. Notice that (7.8) bears a similar form as the popular score-matching objective employed in previous works (**?**Song et al., 2021):

$$L(\theta) := \mathbb{E}\left[\int_0^1 \left\| \nabla \log p(\mathbf{x}_t|\mathbf{x}_0) - s^\theta(X_t, t)\right\|^2 \mathrm{d}t\right], \tag{7.9}$$

where the term $\frac{\mathbf{x}_1 - X_t}{\beta_1 - \beta_t}$ is akin to $\nabla \log p(\mathbf{x}_t|\mathbf{x}_0)$, while $\left(b_t^\theta + \nabla \log h_t^\theta(X_t)\right)$ corresponds to $s^\theta(X_t, t)$.

COMPUTING h_t^θ Inspecting h_t in (7.6), we see that, given $(\mathbf{x}_0, \mathbf{x}_1)$, it can be written as the conditional expectation of an indicator function:

$$h_t(\mathbf{x}) = \mathbb{P}(X_1 = \mathbf{x}_1 | X_t = \mathbf{x}) = \mathbb{E}\left[1_{\{\mathbf{x}_1\}} | X_t = \mathbf{x}\right] \tag{7.10}$$

where the expectation is over (7.5). Functions of the form (7.10) lend itself well to computation since it solves simulating the *unconditioned* paths. Furthermore, in order to avoid overfitting on the given samples, it is customary

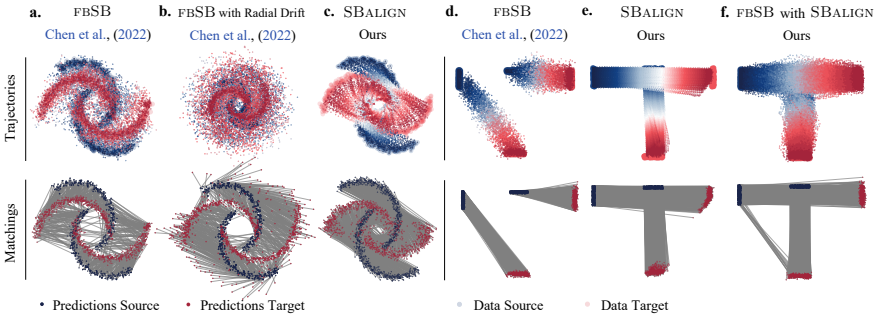

FIGURE 7.2: Experimental results on the Moon dataset (**a-c**) and T-dataset (**d-f**). The top row shows the trajectory sampled using the learned drift, and the bottom row shows the matching based on the learnt drift. Compared to other baselines, SBALIGN is able to learn an appropriate drift respecting the true alignment. (**f**) further showcases the utility of SBALIGN's learnt drift as a suitable reference process to improve other training methods.

to replace the "hard" constraint $1_{\{\mathbf{x}_1\}}$ by its *smoothed* version (**?**Holdijk et al., 2022):

$$h_{t,\lambda}(\mathbf{x}) := \mathbb{E}\left[\exp\left(-\frac{1}{2\lambda}\|X_1 - \mathbf{x}_1\|^2\right)|X_t = \mathbf{x}\right]. \tag{7.11}$$

Here, λ is a regularization parameter that controls how much we "soften" the constraint, and we have $\lim_{\lambda\to 0} h_{t,\lambda} = h_t$.

Although the computation of (7.11) can be done via a standard application of the Feynman–Kac formula (**?**), an altogether easier approach is to parametrize $h_{t,\lambda}$ by a second neural network m^ϕ and perform alternating minimization steps on b_t^θ and m^ϕ. This way, we can also avoid simulating even the unconditional paths of (7.5), and thereby further reducing the variance in training.

REGULARIZATION Since it is well-known that $\nabla \log h_t$ typically explodes when $t \to 1$ (**?**), it is important to regularize the behavior of m^ϕ for numerical stability, especially when $t \to 1$. Moreover, in practice, it is desirable to learn a drift b_t^θ that respects the data alignment *in expectation*: If $(\mathbf{x}_0, \mathbf{x}_1)$ is an input pair, then multiple runs of the SDE (7.5) starting from $\mathbf{x}_0$ should, on average, produce samples that are in the proximity of $\mathbf{x}_1$. This observation implies that we should search for drifts whose corresponding h-transforms are diminishing.

A simple way to simultaneously achieve the above two requirements is to add an ℓ^2-regularization term, resulting in the loss function:

$$L(\theta, \phi) := \mathbb{E}\left[\int_0^1 \left\| \frac{\mathbf{x}_1 - X_t}{\beta_1 - \beta_t} - \left(b_t^\theta + m^\phi(X_t)\right)\right\|^2 + \lambda_t \|m^\phi(\mathbf{x}_t)\|^2 \, \mathrm{d}t\right] \tag{7.12}$$

where λ_t can either be constant or vary with time. The overall algorithm is depicted in algorithm 1.

7.1.2 *Paired Schrödinger Bridges as Prior Processes*

Classical SBs are unsuitable in cases where the alignments are known, because they only consider samples from $\hat{\mathbb{P}}_0$ and $\hat{\mathbb{P}}_1$ and disregard those drawn from the (optimal) coupling $\pi^\star$. However, the reliance of our method on this crucial knowledge is critical to avoid the necessity of IPF-like iterates but may become a limitation when insufficient information on alignments is available.

In such a situation, while it is unrealistic to hope for an accurate solution to the aligned SB problem, the interpolation between $\hat{\mathbb{P}}_0$ and $\hat{\mathbb{P}}_1$ learned by SBALIGN (7.5) can potentially still be leveraged to obtain a better reference process, when solving a classical SB on the same marginals —i.e. the term $b_t(X_t)$ learned via SBALIGN can, in fact, be used *as is* to construct a data-informed alternative $\tilde{\mathbb{Q}}_t$ to the standard Brownian motion (7.2).

Improved reference processes, either using pre-trained or data-informed ones, have been previously considered in the literature. For instance, both De Bortoli et al. (2021) and Chen et al. (2022a) use a pre-trained reference process for challenging image interpolation tasks. This approach, however, relies on DSBs trained using the classical score-based generative modeling objective between a Gaussian and the data distribution. It therefore pre-trains the reference process on a related —but different— process, i.e., the one mapping Gaussian noise to data rather than $\hat{\mathbb{P}}_0$ to $\hat{\mathbb{P}}_1$. An alternative, proposed by Bunne et al. (2023), draws on the closed-form solution of SBs between two Gaussian distributions, which are chosen to approximate $\hat{\mathbb{P}}_0$ and $\hat{\mathbb{P}}_1$, respectively. Unlike our method, these alternatives construct better prior drifts by falling back to simpler and related tasks, or approximations of the original problem. We instead propose to shape a coarse-grained description of the drift based on alignments sampled directly from $\mathbb{P}_{0,1}$.

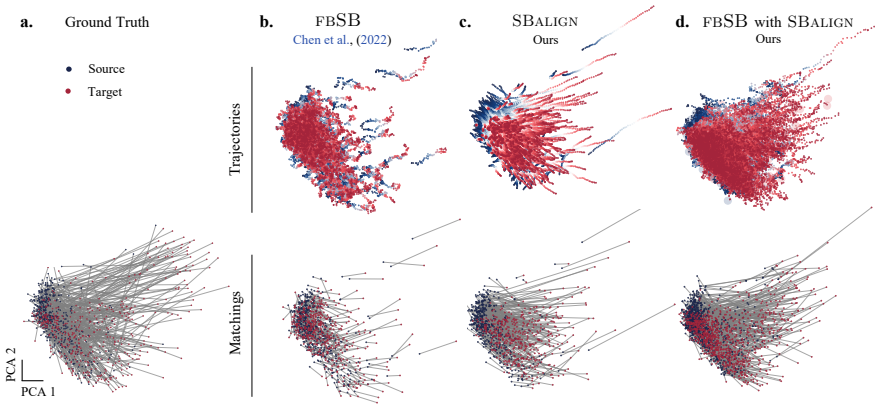

FIGURE 7.3: Cell differentiation trajectories based on (**a**) the ground truth and (**b-d**) learned drifts. SBALIGN is able to learn an appropriate drift underlying the true differentiation process while respecting the alignment. (**d**) Using the learned drift from SBALIGN as a reference process helps improve the drift learned by other training methods.

7.2 EMPIRICAL EVALUATION

In this section, we evaluate SBALIGN in different settings involving 2-dimensional synthetic datasets, the task of reconstructing cellular differentiation processes, as well as predicting the conformation of a protein structure and its ligand formalized as rigid protein docking problem.

7.2.1 *Synthetic Experiments*

We run our algorithm on two synthetic datasets (figures in § **??**), and compare the results with classic Schrödinger bridge models, i.e., the forward-backward SB formulation proposed by Chen et al. (2022a), herein referred to as FBSB. We equip the baseline with prior knowledge, as elaborated below, to further challenge SBALIGN.

MOON DATASET The first synthetic dataset (Fig. 7.2a-c) consists of two distributions, each supported on two semi-circles ($\hat{\mathbb{P}}_0$ drawn in *blue* and $\hat{\mathbb{P}}_1$ in *red*). $\hat{\mathbb{P}}_1$ was obtained from $\hat{\mathbb{P}}_0$ by applying a clockwise rotation around the center, i.e., by making points in the upper blue arm correspond to those in the right red one. This transformation is clearly not the most likely

one under the assumption of Brownian motion of particles and should therefore not be found as the solution of a classical SB problem. This is confirmed by FBSB trajectories (Fig. 7.2a), which tend to map points to their closest neighbor in $\hat{\mathbb{P}}_1$ (e.g., some points in the upper arm of $\hat{\mathbb{P}}_0$ are brought towards the left rather than towards the right). While being a minimizer of (SB), such a solution completely disregards our prior knowledge on the alignment of particles, which is instead reliably reproduced by the dynamics learned by SBALIGN (Fig. 7.2b).

One way of encoding this additional information on the nature of the process is to modify $\mathbb{Q}_t$ by introducing a clockwise radial drift, which describes the prior tangential velocity of particles moving circularly around the center. Solving the classical SB with this updated reference process indeed generates trajectories that respect most alignments (Fig. 7.2b), but requires a hand-crafted expression of the drift that is only possible in very simple cases.

T DATASET In most real-world applications, it is very difficult to define an appropriate reference process $\mathbb{Q}_t$, which respects the known alignment without excessively distorting the trajectories from a solution to (SB). This is already visible in simple examples like (Fig. 7.2d-f), in which the value of good candidate prior drifts at a specific location needs to vary wildly in time. In this dataset, $\hat{\mathbb{P}}_0$ and $\hat{\mathbb{P}}_1$ are both bi-modal distributions, each supported on two of the four extremes of an imaginary T-shaped area. We target alignments that connect the two arms of the T as well as the top cloud with the bottom one. We succeed in learning them with SBALIGN (Fig. 7.2e) but unsurprisingly fail when using the baseline FBSB (Fig. 7.2d) with a Brownian motion prior.

In this case, however, attempts at designing a better reference drift for FBSB must take into account the additional constraint that the horizontal and vertical particle trajectories intersect (see Fig. 7.2e), i.e., they cross the same area at times t_h and t_v (with $t_h > t_v$). This implies that the drift b_t, which initially points downwards (when $t < t_v$), should swiftly turn rightwards (for $t > t_h$). Setting imprecise values for one of t_h and t_v when defining custom reference drifts for classical SBs would hence not lead to the desired result and, worse, would actively disturb the flow of the other particle group.

As described in § 7.1.2, in presence of hard-to-capture requirements on the reference drift, the use of SBALIGN offers a remarkably easy and efficient way of learning a parameterization of it. For instance, when using the

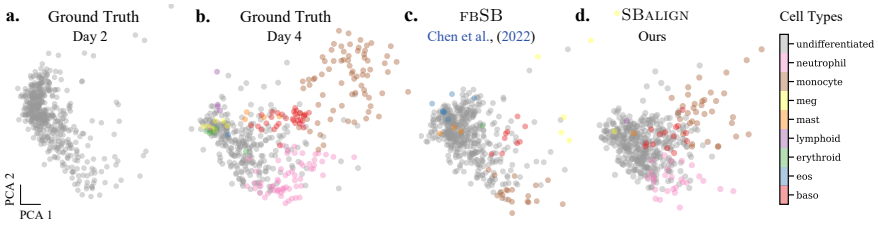

FIGURE 7.4: Cell type prediction on the differentiation dataset. All distributions are plotted on the first two principal components. **a-b:** Ground truth cell types on day 2 and day 4 respectively. **c-d:** FBSB and SBALIGN cell type predictions on day 4. SBALIGN is able to better model the underlying differentiation processes and capture the diversity in cell types.

drift obtained by SBALIGN as reference drift for the computation of the SB baseline (FBSB), we find the desired alignments (Fig. 7.2f).

7.2.2 *Cell Differentiation*

Biological processes are determined through heterogeneous responses of single cells to external stimuli, i.e., developmental factors or drugs. Understanding and predicting the dynamics of single cells subject to a stimulus is thus crucial to enhance our understanding of health and disease and the focus of this task. Most single-cell high-throughput technologies are destructive assays —i.e., they destroy cells upon measurement— allowing us to only measure *unaligned* snapshots of the evolving cell population. Recent methods address this limitation by proposing (lower-throughput) technologies that keep cells alive after transcriptome profiling (Chen et al., 2022b) or that genetically tag cells to obtain a clonal trace upon cell division (Weinreb et al., 2020).

DATASET To showcase SBALIGN's ability to make use of such (partial) alignments when inferring cell differentiation processes, we take advantage of the genetic barcoding system developed by Weinreb et al. (2020). With a focus on fate determination in hematopoiesis, Weinreb et al. (2020) use expressed DNA barcodes to clonally trace single-cell transcriptomes over time. The dataset consists of two snapshots: the first, recorded on day 2, when most cells are still undifferentiated (see Fig. 7.4a), and a second, on day 4, comprising many different mature cell types (see Fig. 7.4b). Using SBALIGN as well as the baseline FSSB, we attempt to reconstruct cell

	Cell Differentiation				
Methods	MMD ↓	W_ε ↓	ℓ_2(PS) ↓	RMSD ↓	Class. Acc. ↑
FBSB	1.58e-2	12.6	4.07	9.63e-1	58.0%
FBSB with SBALIGN	5.15e-3	10.6	0.95	9.88e-1	49.0%
SBalign	9.77e-3	11.2	1.24	9.28e-1	56.0%

TABLE 7.1: **Cell differentiation prediction results.** Shown are distributional metrics (MMD, W_ϵ), alignment-based metrics (ℓ_2, RMSD), and cell type classification accuracy for different methods on the cell differentiation dataset.

evolution between day 2 and day 4, all while capturing the heterogeneity of emerging cell types. For details on the dataset, see § **??**.

BASELINES We benchmark SBALIGN against previous DSB such as (Chen et al., 2022a, FBSB). Beyond, we compare SBALIGN in the setting of learning a prior reference process. Naturally, cell division processes and subsequently the propagation of the barcodes are very noisy. While this genetic annotation provides some form of assignment, it does not capture the full developmental process. We thus test SBALIGN in a setting where it learns a prior from such partial alignments and, plugged into FBSB, is fine-tuned on the full dataset.

EVALUATION METRICS To assess the performance of SBALIGN and the baselines, we monitor several metrics, which include distributional distances, i.e., MMD (Gretton et al., 2012) and W_ϵ (Cuturi, 2013), as well as average scores, i.e., ℓ_2(PS) (Bunne et al., 2021) and RMSD. Moreover, we also train a simple neural network-based classifier to annotate the cell type on day 4 and we report the accuracy of the predicted vs. true cell type for all the models. See § **??** for further details.

RESULTS SBALIGN accurately predicts cellular differentiation processes in hematopoiesis from day 2 to day 4, as visible from the (2D projections of the) learned trajectories and alignments (Fig. 7.3c) and the quantitative evaluation in Table 7.1. SBALIGN outperforms FBSB in all but the cell-type accuracy metric: Remarkably, our method exceeds the performances of the baseline also on distributional metrics and not uniquely on alignment-based ones. Further, we evaluate how well SBALIGN recovers the heterogeneity

of emerging cell types throughout the developmental process on day 4. The results are displayed in Fig. 7.4d and show that, while capturing the overall differentiation trend, SBALIGN (as well as FBSB) struggles to isolate rare cell types. Lastly, we employ SBALIGN to learn a prior process from noisy alignments based on genetic barcode annotations. When using this reference process within FBSB, we learn an SB which compensates for inaccuracies stemming from the stochastic nature of cell division and barcode redistribution and which achieves better scores on distributional metrics (see Tab. 7.1). Further results can be found in § **??**.

7.3 CONCLUSION

In this paper, we propose a new framework to tackle the interpolation task with aligned data via DSB. Our central contribution is a novel algorithmic framework derived from the Schrödinger bridge theory and Doob's *h*-transform. Via a combination of the two notions, we derive novel loss functions which, unlike all prior methods for solving DSB, do not rely on the IPF procedure and are hence numerically stable. We verify our proposed algorithm on various synthetic and real-world tasks and demonstrate noticeable improvement over the previous state-of-the-art, thereby substantiating the claim that data alignment is a highly relevant feature that warrants further research.

8

...

Ein solches mathematisch-definierbares System ist überhaupt nicht die Wirklichkeit selbst, sondern nur ein Schema, welches zur Beschreibung der Wirklichkeit dienen kann.

— Andrey Kolmogorov, *Über die analytischen Methoden in der Wahrscheinlichkeitsrechnung* (1931)

MODELING PARTICLE DYNAMICS AS A JKO SCHEME. In this paper, we draw inspiration from both approaches above—the intuition from the recent NF literature that flows should mimic an optimal transport (OT as prior), and be able, through training, to predict future configurations (OT as a loss)—to propose a causal model for population dynamics. Our approach relies on a powerful hammer: the Jordan-Kinderlehrer-Otto (JKO) flow (Jordan et al., 1998), widely regarded as one of the most influential mathematical breakthroughs in recent history. While the JKO flow was initially introduced as an alternative method to solve the Fokker-Planck partial differential equation (PDE), its flexibility can be showcased to handle more complex PDEs (Santambrogio, 2017, §4.7), or even describe the gradient flows of non-differentiable energies that have no PDE representation. On a purely mechanical level, a JKO step is to measures what the proximal step (Combettes and Pesquet, 2011) is to vectors: In a JKO step, particles move to decrease collectively an *energy* (a real-valued function defined on measures), yet remain close (in Wasserstein sense) to the previous configuration. Our goal in this paper is to treat JKO steps as parameterized modules, and fit their parameter (the energy function) so that its outputs agree repeatedly over time with observed data. This approach presents several challenges: While numerical approaches to solve JKO steps have been proposed in low dimensional settings (Burger et al., 2010; Carrillo et al., 2021; Peyré, 2015; Benamou et al., 2016a), scaling it to higher dimensions is an open problem. Moreover, minimizing a loss involving a JKO step w.r.t. energy requires not only solving the JKO problem, but also computing the (transpose) Jacobian of its output w.r.t. energy parameters.

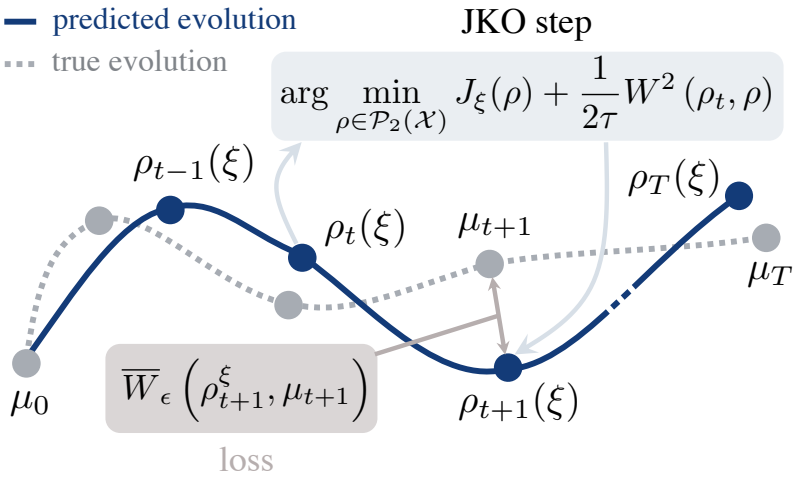

FIGURE 8.1: Given an observed trajectory $(\mu_0, \dots, \mu_T)$ of point clouds (gray), we seek parameters ξ for the energy J_ξ such that the predictions $\rho_1, \dots, \rho_T$ (blue) following a JKO flow from $\rho_0 = \mu_0$ are close the observed trajectory (gray), by minimizing (as a function of ξ) the sum of Wasserstein distances between ρ_{t+1}, the JKO step from ρ_{t-1} using J_ξ, and data μ_{t+1}.

CONTRIBUTIONS. Our contributions are two-fold. First, we propose a method, given an input configuration and an energy function, to compute JKO steps using input convex neural networks (ICNN) (Amos et al., 2017; **?**) (see also concurrent works that have proposed similar approaches (Alvarez-Melis et al., 2021; Mokrov et al., 2021)). Second, we view the JKO step as an inner layer, a JKONET module parameterized by an energy function, which is tasked with moving the particles of an input configuration along an OT flow (the gradient of an optimal ICNN), trading off a lower energy with proximity to the previous configuration. We propose to estimate the parameters of the energy by minimizing a fitting loss computed between the outputs of the JKONET module (the prediction) and the ground truth displacements, as illustrated in Figure 8.1. We demonstrate JKONET's range of applications by applying in on synthetic potential- and trajectory-based population dynamics, as well as developmental trajectories of human embryonic stem cells based on single-cell genomics data.

8.1 BACKGROUND

JKO FLOWS. In their seminal paper, Jordan et al. (1998) study diffusion processes under the lens of the OT metric (see also Ambrosio et al., 2006) and introduce a scheme that is now known as the JKO flow: Starting with ρ_0, and given a real-valued energy function $J : \mathcal{P}(\mathbb{R}^d) \to \mathbb{R}$ driving the evolution of the system, they define iteratively for $t \geq 0$, :

$$\rho_{t+1} = \arg\min_{\rho \in \mathcal{P}_2(\mathbb{R}^d)} J(\rho) + \frac{1}{2\tau} W^2(\rho, \rho_t)\,, \tag{8.1}$$

where τ is a time step parameter. These successive minimization problems result in a sequence of probability measures in $\mathcal{P}(\mathbb{R}^d)$. The JKO flow can thus be seen as the analogy of the usual proximal descent scheme, tailored for probability measures (Santambrogio, 2015, p.285). Jordan et al. (1998) show that as step size $\tau \to 0$, and for a specific energy J that is the sum of a linear term and the negentropy, the measures describing the JKO flow recover solutions to a Fokker-Planck equation. In this work, following in the footsteps of more general applications of the JKO scheme (Santambrogio, 2017, §4.8), we model dynamics without necessarily having in mind PDE solutions in mind, to interpret instead the JKO step as a more general parametric type of dynamic for probability measures, exclusively parameterized by the energy J itself.

8.2 PROXIMAL OPTIMAL TRANSPORT MODEL

Given T discrete measures $\mu_0, \ldots, \mu_T$ describing the time evolution of a population, we posit that such an evolution follows a JKO flow for the free energy functional J, and assume that energy does not change throughout the dynamic. We parameterize the energy J as a neural network with parameters ξ, and fit ξ so that the JKO flow model matches the observed data.

Fitting parameter ξ with a reconstruction loss requires, using the chain rule, being able to differentiate the JKO step's output w.r.t. ξ (see Fig. 8.1), and more precisely provide a way to apply that transpose Jacobian to an arbitrary vector when using reverse-mode differentiation. To achieve this, we introduce a novel approach to numerically solve JKO flows using ICNNs (§ 8.2.1), resulting in a bilevel optimization problem targeting the energy J_ξ (§ 8.2.2).

8.2.1 *Reformulation of JKO Flows via ICNNs*

Given a starting condition ρ_t and energy functional J_ξ, the JKO step consists in producing a new measure ρ_{t+1} implicitly defined as the minimizer of (8.1). Solving directly (8.1) on the space of measures, involves substantial computational costs. Different numerical schemes have been developed, e.g., based notably on Eulerian discretization of measures (Carrillo et al., 2021; Benamou et al., 2016b), and/or entropy-regularized optimal transport (Peyré, 2015). However, these methods are limited to small dimensions since the cost of discretizing such spaces grows exponentially. Except for the Eulerian approach proposed in (Peyré, 2015), obtained as the fixed point of a Sinkhorn type iteration, the differentiation would also prove extremely challenging as a function of the energy parameter ξ.

To reach scalability and differentiability, we build upon the approach outlined in Benamou et al. (2016b) to reformulate the JKO scheme as a problem solved over convex functions, rather than on measures ρ. Effectively, this is equivalent to making a change of variables in (8.1): Introduce a (variable) convex function ψ, and replace the variable ρ by the variable $\nabla\psi_\# \rho_t$. Writing

$$\mathcal{E}_J(\rho, \nu) := J(\rho) + \frac{1}{2\tau} W_2^2(\rho, \nu), \tag{8.2}$$

this identity states that, assuming μ and ν being absolutely continuous w.r.t. Lebesgue measure that

$$\min_\rho \mathcal{E}_J(\rho, \nu) = \min_{\psi \text{ convex}} \mathcal{F}_J(\psi, \nu) := \mathcal{E}_J(\nabla\psi_\# \nu, \nu)\,,$$

simplifying the Wasserstein term in (8.2), using the assumption that ψ is convex and Brenier's theorem (§ **??**):

$$\mathcal{F}_J(\psi, \nu) = J(\nabla\psi_\# \nu) + \frac{1}{2\tau} \int \|x - \nabla\psi(x)\|^2 d\nu(x) \tag{8.3}$$

We pick an ICNN architecture to optimize over a restricted family of convex functions, $\{\psi_\theta\}$, and define, starting from $\rho_0(\xi) := \mu_0$, the recursive sequence for $t \geq 0$,

$$\rho_{t+1}(\xi) := \nabla\psi_{\theta^\star(\xi, \rho_t(\xi))\#}\, \rho_t(\xi)\,, \tag{8.4}$$

with $\theta^\star(\xi, \rho_t)$ defined implicitly using ξ and any ν as

$$\theta^\star(\xi, \nu) := \arg\min_\theta \mathcal{F}_J(\psi_\theta, \nu) \tag{8.5}$$

STRONG CONVEXITY OF ψ_θ. The strong convexity and smoothness of a potential ψ impacts the regularity of the corresponding OT map $\nabla\psi$ (Caffarelli, 2000; Figalli, 2010), since one can show that for a ℓ-strongly convex, L-smooth ψ one has (Paty et al., 2020) that

$$\ell\|x-y\| \leq \|\nabla\psi(x) - \nabla\psi(y)\| \leq L\|x-y\|.$$

While it is more difficult to enforce the L-smoothness of a neural network, and more generally its Lipschitz constants (Scaman and Virmaux, 2018) it is easy to enforce its strong convexity, by simply adding a term $\ell\|x\|^2/2$ to the corresponding potential, or a residual rescaled term ℓx to the output $\nabla\psi(x)$. This approach can be used to enforce that the push-forward of the gradient of an ICNN does not collapse to a single point, maintaining spatial diversity.

8.2.2 *Learning the Free Energy Functional*

The energy function $J_\xi : \mathcal{P}(\mathbb{R}^d) \to \mathbb{R}$ can be any parameterized function taking a measures as an input. Since our model assumes that the observed dynamic is parameterized entirely by that energy (and the initial observation ρ_0), the more complex this dynamic, the more complex one would expect the energy J_ξ to be. We focus in this first attempt on linear functions in the space of measures, that is expectations over ρ of a vector-input neural network E_ξ

$$J_\xi(\rho) := \int E_\xi(x) d\rho(x), \tag{8.6}$$

where $E_\xi : \mathbb{R}^d \to \mathbb{R}$ is a multi-layer perceptron (MLP).

Algorithm 2 JKONET Algorithm.

Input: Dataset $\mathcal{D} = \{\{\mu_t^0\}_{t=0}^T, \ldots, \{\mu_t^N\}_{t=0}^T\}$ of N population trajectories, ξ^0 energy parameter initialization, θ^0 ICNN parameter initialization, learning rates lr_θ and lr_ξ, step τ, regularizer ε, tolerance α, `TeacherForcing` flag.

Output: Free energy J_ξ explaining underlying population dynamics of snapshot data.

$\xi \leftarrow \xi^0$
for $\{\mu_t\}_{t=0}^T \in \mathcal{D}$ **do**
  for $t \leftarrow 0$ ***to*** $T-1$ **do**
    $\theta \leftarrow \theta^0$
    if *TeacherForcing* **then**
      $\nu \leftarrow \mu_t$
    else
      $\nu \leftarrow \rho_t(\xi)$
    while $\frac{\sum_i \|\nabla_{\theta_i} \mathcal{F}_{J_\xi}(\theta)\|_2}{\sum_i count(\theta_i)} \geq \alpha$ **do**
      $\theta \leftarrow \theta - \mathrm{lr}_\theta \times \nabla_\theta \mathcal{F}_{J_\xi,\nu}(\theta)$
    $\rho_{t+1}(\xi) \leftarrow \nabla\psi_{\theta\#}\nu$
  $\xi \leftarrow \xi - \mathrm{lr}_\xi \times \nabla_\xi \overline{W}_\varepsilon(\rho_{t+1}(\xi), \mu_{t+1})$
return J_ξ

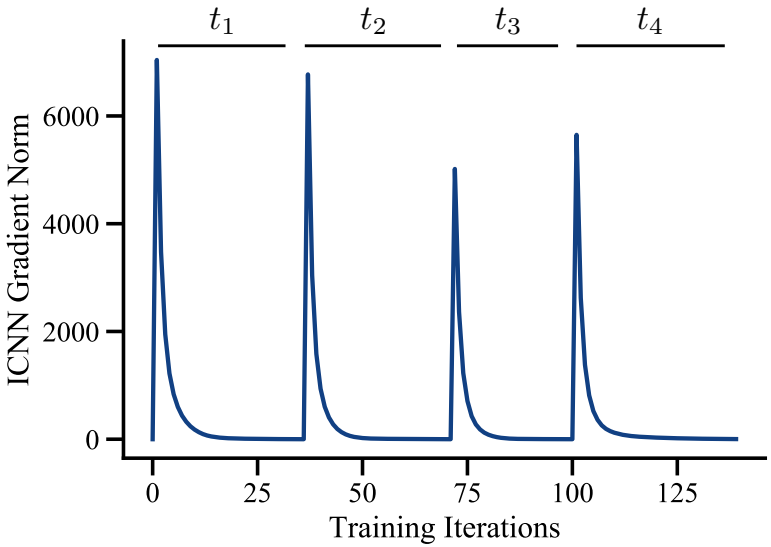

FIGURE 8.2: Optimization of the ICNN used in JKO steps. The bumps correspond to a change in the outer iteration, the smooth decrease in between

Inferring nonlinear energies accounting for population growth and decline, as well as interactions between points, using the formalism of (De Bie et al., 2019), transformers (Vaswani et al., 2017) or set pooling methods (Edwards and Storkey, 2017; Zaheer et al., 2017), is an exciting direction for future work.

To address slow convergence and instabilities for dynamics with many snapshots, we use teacher forcing (Williams and Zipser, 1989) to learn J_ξ through time. In those settings, during training, J_ξ uses the ground truth as input instead of predictions from the previous time step. At test time, we do not use teacher forcing.

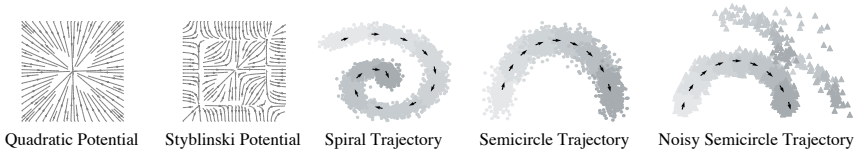

FIGURE 8.3: Overview on different tasks including trajectory- and potential-based dynamics.

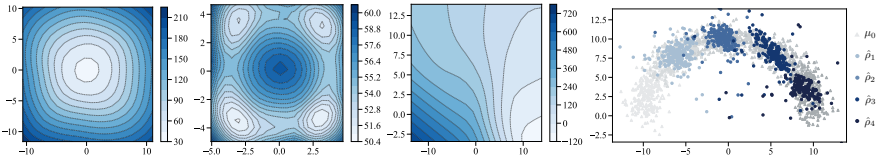

(a) Quadratic Potential.

(b) Styblinski Potential.

(c) Semicircle Trajectory *with* teacher forcing.

(d) Predicted Population Evolution on Semicircle Trajectory.

FIGURE 8.4: **Results of JKOnet on Potential- and Trajectory-based Dyanamics.** (a)-(c) Contour plots of the energy functionals J_ξ of JKONET on potential- and trajectory-based population dynamics in different training settings (i.e., trained with or without teacher forcing § 8.2.2), color gradients depict the magnitude of J_ξ. (d) Predicted population snapshots $(\hat{\rho}_1, \ldots, \hat{\rho}_4)$ (blue) and data trajectory $(\mu_0, \ldots, \mu_4)$ (gray).

8.2.3 *Bilevel Formulation of* JKONET

Learning the free energy functional J_ξ while solving each JKO step via an ICNN results in a challenging bilevel optimization problem. At each time

step, the predicted dynamics are compared to the ground truth trajectory $(\mu_0, \mu_1, \ldots, \mu_T)$ with a Sinkhorn loss (2.3),

$$\begin{aligned} &\min_{\xi} \sum_{t=0}^{T-1} \overline{W}_\varepsilon(\rho_{t+1}(\xi), \mu_{t+1}), \\ &\text{s.t. } \rho_0(\xi) := \mu_0, \\ &\qquad \rho_{t+1}(\xi) := \nabla\psi_{\theta^\star} \# \rho_t(\xi)\,, \\ &\qquad \theta^\star := \arg\min_{\theta} \mathcal{F}_{J_\xi}(\psi_\theta, \rho_t(\xi)) \end{aligned} \tag{8.7}$$

The dependence of the Sinkhorn divergence losses in (8.7) on ξ only appears in the fact that the predictions $\rho_{t+1}(\xi)$ are themselves implicitly defined as solving a JKO step parameterized with the energy J_ξ. Learning J_ξ through the exclusive supervision of data observations requires therefore to differentiate the arg-minimum of a JKO problem, down therefore through to the lower-level optimization of the ICNN. We achieve this by implementing a differentiable double loop in `JAX`, differentiating first the Sinkhorn divergence using the `OTT`[1] package (Cuturi et al., 2022), and then backpropagating through the ICNN optimization by unrolling Adam steps (Kingma and Ba, 2014; Metz et al., 2017; Lorraine et al., 2020).

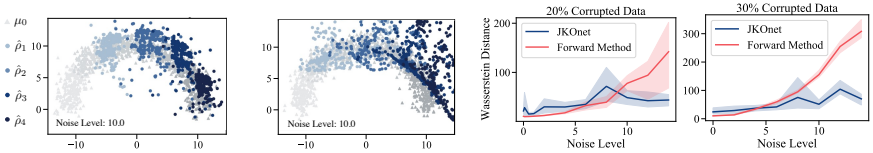

(a) JKONET on 30% corrupted data.

(b) Forward method on 30% corrupted data.

(c) W_ϵ (2.2) vs. noise level on 20% corrupted data.

(d) W_ϵ (2.2) vs. noise level on 30% corrupted data.

FIGURE 8.5: Comparison between JKONET and the forward method in settings of increasing noise on corrupted data on the semicircle trajectory task.

1 github.com/ott-jax/ott

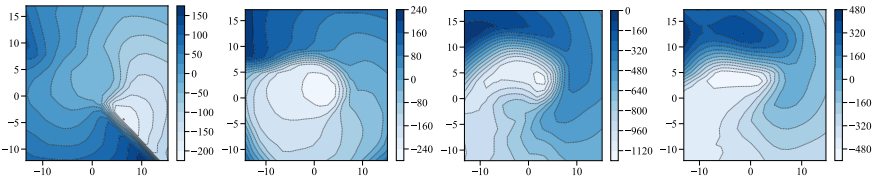

(a) Forward method, *with* teacher forcing.

(b) Forward method, *no* teacher forcing.

(c) JKONET, *with* teacher forcing.

(d) JKONET, *no* teacher forcing.

FIGURE 8.6: Comparison between energy functionals J_ξ of the spiral trajectory task (see 8.3) between the forward method and JKONET, trained with or without teacher forcing § 8.2.2). When using teacher forcing, the forward method overfits a gap on the lower-right corner of the spiral, outputting a highly irregular energy. When taking into account the entire trajectory recursively, the Forward method does better overall, but is unable to recover an energy as precise as that returned by JKONET.

INNER LOOP TERMINATION. A question that arises when defining $\rho_{t+1}(\xi)$ lies in the budget of gradient steps needed or allowed to optimize the parameters θ of the ICNN, before taking a new gradient step on ξ in the outer loss. A straightforward approach in `JAX` (Bradbury et al., 2018) would be to use a preset number of iterations with a `for` loop (`jax.lax.scan`). We do observe, however, that the number of iterations needed to converge in relevant scenarios can vary significantly with the ICNN architecture and/or the hardness of the underlying task. We propose to use instead a differentiable fixed-point loop to solve each JKO step up to a desired convergence threshold. We measure convergence of the optimization of the ICNN via the average norm of the gradient of the JKO objective w.r.t. the ICNN parameters θ, i.e., $\sum_i \|\nabla_{\theta_i} \mathcal{F}_{J_\xi}(\theta_i, \xi)\|_2 / \sum_i \text{count}(\theta_i)$. We observe that this approach is robust across datasets and architectures of the ICNN. An exemplary training curve for the ICNNs updated successively along a time sequence is shown in Figure 8.2.

REVERSE-MODE DIFFERENTIATION. The Jacobian $\partial \rho_{t+1} / \partial \xi$ arising when computing the gradient $\nabla_\xi \overline{W}_\varepsilon(\rho_{t+1}(\xi), \mu_{t+1})$ is obtained by unrolling the while loop above. The gradient term of the Sinkhorn divergence w.r.t the first argument is given by the Danskin envelope theorem (Danskin, 1967).

Method	Prediction Loss (W_ε)			
	Day 6 to 9	Day 12 to 15	Day 18 to 21	Day 24 to 27
One-Step Ahead				
Forward Method	0.187 ± 0.001	0.162 ± 0.010	0.185 ± 0.020	0.203 ± 0.004
JKONET	$\mathbf{0.133 \pm 0.020}$	$\mathbf{0.133 \pm 0.008}$	$\mathbf{0.172 \pm 0.0130}$	$\mathbf{0.169 \pm 0.004}$
All-Steps Ahead				
Forward Method	0.225 ± 0.023	0.160 ± 0.001	0.171 ± 0.016	0.183 ± 0.007
JKONET	$\mathbf{0.148 \pm 0.015}$	$\mathbf{0.144 \pm 0.013}$	$\mathbf{0.154 \pm 0.024}$	$\mathbf{0.138 \pm 0.034}$

TABLE 8.1: Evaluation of predictive performance w.r.t. the entropy-regularized Wasserstein distance W_ε (2.2) of JKONET and the forward method on the embryoid body scRNA-seq data per time step (using 3 runs).

SETTING τ IN (**??**). In usual JKO applications, τ needs to be tuned manually. In this work, the energy J_ξ is not fixed, but trained to fit data. Since we put no constraints on the scaling of J_ξ, τ can be set to 1 without loss of generality, as the parameter ξ will automatically adjust so that the scale of J_ξ induces steps of a relevant length to fit data. This only holds (as with a usual JKO step) if the trajectories are sampled regularly. For irregularly spaced time series, τ can be adapted at train and test time to the spacing of timestamps (shorter steps requiring larger τ).

8.3 EVALUATION

In the following, we evaluate our method empirically on a variety of tasks. This includes recovering synthetic potential- and trajectory-based population dynamics (see Fig. 8.3), as well as the evolution of high-dimensional single-cell populations during a developmental process.

8.3.1 *Synthetic Population Dynamics*

ENERGY-DRIVEN TRAJECTORIES. The first task involves evolutions of partial differential equations with known potential. We hereby consider both convex (e.g., the quadratic function $J(x) = \|x\|_2^2$) and nonconvex potentials (e.g., Styblinski function) (see Fig. 8.3). These two-dimensional synthetic flows are generated using the Euler-Maruyama method (Kloeden and Platen, 1992). For details, see § **??**. To recover the true potential via JKONET, we parameterize both energy J_ξ and ICNN ψ_θ with linear layers ($\epsilon = 1.0$, $\tau = 1.0$, § **??**). More details on the architectures can be found

in § **??**. Figure 8.4a-b demonstrate JKONET's ability to recover convex and nonconvex potentials via energy J_ξ.

ARBITRARY TRAJECTORIES. As a sanity check, we evaluate if JKONET can recover an energy functional J_ξ from trajectories that are not necessarily arising from the gradient of an energy. Here, a 2-dimensional Gaussian moves along a predefined trajectory with nonconstant speed. For details on the data generation, see § **??**. We consider a line, a spiral, and movement along a semicircle (Fig. 8.3). As visible in Figure 8.4c (5 snapshots), Figure **??**b (2 snapshots), and Figure 8.6c-d (10 snapshots), JKONET learns energy functionals J_ξ that can then model the ground truth trajectories. These trajectory-based dynamics are learned using the strong convexity regularizer ($\ell = 0.8$, see § 8.2.1).

COMPARISON TO FORWARD METHODS. Instead of parameterizing the next iteration $\rho_{t+1}(\xi)$ as we do in the JKONET formulation (8.1), the *forward* scheme states that the prediction at time $t+1$, η_{t+1}, can be obtained as $(\nabla F_\xi)_\# \eta_t(\xi)$, where F_ξ is any arbitrary neural network, as considered in Hashimoto et al. (2016), namely $\eta_0 := \mu_0$ and subsequently $\eta_{t+1}(\xi) := (\nabla F_\xi)_\# \eta_t(\xi)$. Although OT still plays an important role in that paper, since the potential F is estimated by minimizing a Sinkhorn loss $\overline{W}_\varepsilon(\eta_{t+1}, \mu_{t+1})$, as we do in (8.7), the forward displacement operator $(\nabla F_\xi)_\#$ has no spatial regularity. Because of that, we observe that the forward method can get more easily trapped in local minima, and, in particular, overfits the training data (see § **??**) as shown by a substantial decrease in performance in the presence of noise. We demonstrate this in different scenarios: First, we compare the robustness of both JKONET and the forward method to noise. For this, we corrupt 20% or 30% of the training data on the example of the semicircle trajectory with different levels of noise (see Fig. 8.3). We insist that noise is only added at training time, as random shifts on both feature dimensions, while we test on the original semicircle trajectory. In low noise regimes, where train and test data are similar, the forward method overfits and performs marginally better than JKONET (see Fig. 8.5c,d). As noise increases, the performance of the forward method deteriorates (Fig. 8.5b), while JKONET, constrained to move points with OT maps, is robust (Fig. 8.5a).

In a second experiment, we evaluate the capacity of JKONET and the forward method to extrapolate and generalize the learned trajectories, e.g., when vertically translating a line during test time (Fig. **??**). Due to

the less constrained energy, the *forward* method perfectly resembles the seen trajectory during training, but fails to extrapolate to shifted test data (Table **??** in § **??**).

Lastly, we compare the resulting energy functionals F_ξ and J_ξ of the forward method and JKONET, respectively, on the spiral trajectory (see Fig. 8.6). When learning long and complex population dynamics, teacher forcing improves training (see additional results in Fig. **??**c-d as well as Fig. 8.4c-d). While facilitating training of the forward method in some settings, it likewise results in wrong energy functionals F_ξ (Fig. 8.6a). JKONET, on the other hand, is able to globally learn the energy functional J_ξ, despite being only exposed to a one-step history of snapshots during training with teacher forcing (see Fig. 8.6c).

8.3.2 *Single-Cell Population Dynamics*

We investigate the ability of JKONET to predict the evolution of cellular and molecular processes through time. The advent of single cell profiling technologies has enabled the generation of high-resolution single-cell data, making it possible to profile individual cells at different states in the development. A key difficulty in learning the evolution of cell populations is that a cell is (usually) destroyed during a measurement. Thus, although one is able to collect features at the level of individual cells, the same cell cannot be measured twice. Instead, we collect independent samples at each snapshot, resulting in *unaligned* distributions across snapshots, without access to ground-truth single-cell trajectories. The goal of learning individual dynamics is to identify ancestor and descendant cells, and get a better understanding of biological differentiation or reprogramming mechanisms.

We apply JKONET to embryoid body single-cell RNA sequencing (scRNA-seq) data (Moon et al., 2019), describing the differentiation of human embryonic stem cells grown as embryoid bodies into diverse cell lineages over a period of 27 days. During this time, cells are collected at 5 different snapshots (day 1 to 3, day 6 to 9, day 12 to 15, day 18 to 21, day 24 to 27) and measured via scRNA-seq (resulting in 15,150 cells). For details on the dataset and data preprocessing see § **??**. We run JKONET as well as the baseline on the first 20 components of a principal component analysis (PCA) of the 4000 highly differentiable genes (see Fig. **??**). We split the dataset into train and test data ($\sim 15\%$) and parameterize both energy J_ξ and ICNN ψ_θ with linear layers ($\epsilon = 1.0$, $\tau = 1.0$, § **??**).

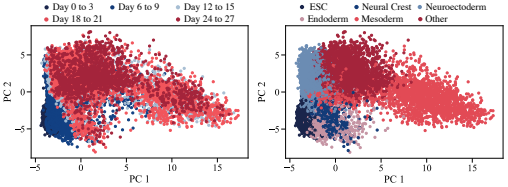

(a) PCA embedding of the embryoid body scRNA-seq data colored by the snapshot time.

(b) PCA embedding of the embryoid body scRNA-seq data colored by the lineage branch class.

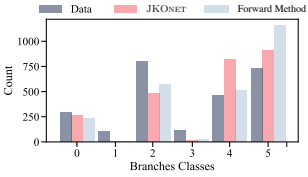

(c) Distribution of cell lineage branch classes in the data or predicted by JKONET or the forward method.

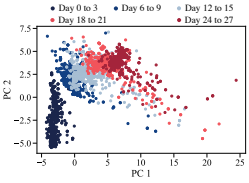

(d) PCA embedding of JKONET predictions colored by the snapshot time.

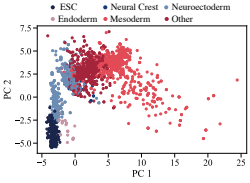

(e) PCA embedding of JKONET predictions colored by the lineage branch class.

Method	Cell Lineage Classification	
	ℓ_1	H^2
One-Step Ahead		
Forward Method	132.27 ± 5.00	0.026 ± 0.002
JKONET	$\mathbf{88.80 \pm 0.57}$	$\mathbf{0.016 \pm 0.001}$
All-Steps Ahead		
Forward Method	$\mathbf{185.47 \pm 12.18}$	0.033 ± 0.002
JKONET	215.60 ± 12.53	0.034 ± 0.004

TABLE 8.3: Evaluation of cell lineage branch classification performance of JKONET and the forward method on the embryoid body scRNA-seq data based on the ℓ_1-distance of the histograms and the Hellinger distance H^2 (8.8) of the predicted branch class distributions (using 3 runs).

CAPTURING SPATIO-TEMPORAL DYNAMICS. Given the samples from the cell population at day 1 to 3 (μ_0), JKONET learns the underlying spatio-temporal dynamics giving rise to the developmental evolution of embryonic stem cells. As no ground truth trajectories are available in the data, we use distributional distances, i.e., the entropy-regularized Wasserstein distance W_ε (2.2) (Flamary et al., 2021), to measure the correctness of the predictions at each time step. We hereby measure the W_ε discrepancy between data and predictions for one-step ahead as well as inference of the entire evolution (all-steps ahead) for each time step t_i, see results in Table 8.1. JKONET outperforms the forward method in terms of W_ε (2.2) distance for both one-step ahead and all-steps ahead predictions for all time steps. The performance of both methods is relatively stable even until day 24 to 27, i.e., the W_ε distance does not significantly grow for future snapshots. We

further visualize the first two principal components of the entire dataset (Fig. 8.7a) and of JKOnet's predictions on the test dataset ($\sim$ 500 cells per snapshot, Fig. 8.7d). Visualization of predictions of the forward method can be found in the Appendix (Fig. **??**a).

CAPTURING BIOLOGICAL HETEROGENEITY. Besides measuring the ability of JKOnet to model and predict the spatio-temporal dynamics of embryonic stem cells, we would like to guarantee, at a more macroscopic level, that JKOnet is also able to learn the cell's differentiation into various cell lineages. Embryoid bodies differentiation covers key aspects of early embryogenesis and thus captures the development of embryonic stem cells (ESC) into the mesoderm, endoderm, neuroectoderm, neural crest and others.

Following Moon et al. (2019, Fig. 6, Suppl. Note 4), we compute lineage branch classes (Fig. **??**c) for all cells based on an initial k-means clustering ($k = 30$) in a 10-dimensional embedding space using PHATE, a non-linear dimensionality reduction method capturing a denoised representation of both local and global structure of a dataset (Fig. **??**b). For details, see § **??**. We then train a k-nearest neighbor (k-NN) classifier ($k = 5$) to infer the lineage branch class based on a 20-dimensional PCA embedding of a cell (classes: ESC: 0, neural crest: 1, neuroectoderm: 2, endoderm: 3, mesoderm: 4, other: 5).

We analyze the captured lineage branch heterogeneity of the population predicted by JKOnet and the forward method by estimating the lineage branch class of each cell using the trained k-NN classifier. The predicted populations colored by the estimated lineage branch as well as the data with the true lineage branch labels are visualized in Figure 8.7e and Figure 8.7b, respectively. The corresponding predicted and true distributions of lineage branch classes are shown in Figure 8.7c. To quantify how well JKOnet and the forward method capture different cell lineage branches, we compute the ℓ_1 distance between the predicted and true histograms as well as the Hellinger distance

$$H^2(a,b) = \frac{1}{2}\sum_{i=1}^{k}\left(\sqrt{a_i/\|a\|_1} - \sqrt{b_i/\|b\|_1}\right)^2 \tag{8.8}$$

between both true and predicted class discrete distributions a and b. Figure 8.7c and Table 8.3 demonstrate that both, JKOnet and the forward method, capture most lineage branches during the differentiation of embryonic stem cells. Both methods, however, have difficulties recovering cells of

the neural crest (class 1) and the endoderm (class 3), lineage branches which are scarcely represented in the original data. The analysis further suggests that both methods reduce in performance w.r.t. biological heterogeneity when predicting the entire trajectory (all-steps ahead), instead of inferring the next snapshot only (one-step ahead).

8.4 CONCLUSION

We proposed JKONET, a model to infer and predict the evolution of population dynamics using a proximal optimal transport scheme, the JKO flow. JKONET solves local JKO steps using ICNNs and learns the energy that parameterizes these steps by fitting JKO flow predictions to observed trajectories using a fully differentiable bilevel optimization problem. We validate its effectiveness through experiments on synthetic potential- and trajectory-based population dynamics, and observe that it is far more robust to noise than a more direct Forward approach. We use JKONET to infer the developmental trajectories of human embryonic stem cells captured via high-dimensional and time-resolved single-cell RNAseq. Our analysis also shows that JKONET captures diverse cell fates during the incremental differentiation of embryonic cells into multiple lineage branches. Using proximal optimal transport to model real complex population dynamics thus makes for an exciting avenue of future work. Extensions could include modeling higher-order interactions among population particles in the energy function, e.g., cell-cell communication.

9

CONCLUSION AND FUTURE DIRECTIONS

It's odd the way life works, the way it mutates and wanders, the way one thing becomes another.
— Siri Hustvedt, *What I Loved* (2003)

In this work we propose CellOT, a framework to model single-cell perturbation responses from unpaired treated and untreated cell states using neural optimal transport. By adequately modeling the nature of the problem through the lens of optimal transport, CellOT determines how perturbations affect cellular properties, reconstructs the most likely trajectory single cells take upon perturbation, and subsequently assists in a better understanding of driving factors of cell fate decision and cellular evasion mechanisms. CellOT builds on the recent successes of optimal transport applications in single-cell biology (Schiebinger et al., 2019b; Lavenant et al., 2021), by introducing a fully parameterized transport map that can be applied to incoming unseen samples. Previous methods (Jacob et al., 2018; Yang and Uhler, 2019; Prasad et al., 2020) rely on an unconstrained parameterization of the *primal* optimal transport map. However, the unconstrained nature of these models makes robust optimization challenging and results in reduced performance (Makkuva et al., 2020, Table 1). Instead, we learn the transformation of unperturbed to perturbed cell states through the *dual* optimal transport problem, parameterized via a pair of neural networks constrained to be convex (Makkuva et al., 2020). These constraints are important inductive biases that facilitate learning and result in a reliable and easy-to-train framework, as evidenced by the consistently strong performance of CellOT on several problems without the need for extensive hyperparameter tuning (see Online Methods).

CellOT infers the highly complex and nonlinear evolution of cell populations in response to perturbations without making strong simplifying assumptions on the nature of these dynamics. Unlike current approaches comprising autoencoder-based baselines (Lopez et al., 2018; Lotfollahi et al., 2019; Yang et al., 2020), CellOT does not necessarily rely on learning meaningful low-dimensional embeddings in which perturbations are modeled as linear shifts. We confirm this advantage through experiments on single-cell responses to different drugs in cancer cell lines obtained with RNA-seq

and spatially resolved 4i measurements, where CellOT consistently outperforms (Fig. **??** and **??**). Our evaluations went beyond the often-used average treatment effect and correlation analysis across all cells; we analyzed marginals and computed MMD scores, a strong measure of how well predicted and observed distributions match.

Using CellOT to perform cell-state-aware drug profiling enables us to quantify perturbation effects as a function of the underlying heterogeneity of the studied system, in our cases a co-culture of two melanoma cell lines with different sensitivities to drug treatments. In doing so, we *sharpen* the response profiles of the measured drugs and reveal cell-state-specific responses of multiple signaling pathway in relation to treatment history of the cell line donor. We find the signaling activity associated to the MEK and PI3k pathways to decouple in cells pre-exposed to MEK inhibitors, a known adaptation mechanism for therapy evasion in melanoma cells (Kun et al., 2021). This *pathway rewiring* is associated to alteration in the molecular feedback structure of cells from effectors to receptors (Kun et al., 2021; Turke et al., 2012). Thus, combining CellOT with a larger set of combination treatments, multiplexed imaging, and cellular systems reflective of disease adaptations may help us to elucidate the molecular mechanisms of signaling pathway evolution in the context of cancer therapy.

We further analyze how well the learned maps generalize beyond samples used for training (o.o.s. setting) and to different sample compositions (o.o.d. setting). In Fig. **??**, we therefore test CellOT's ability to to predict treatment responses in unseen lupus patients, infer developmental trajectories on stem cells of lower potency, and translate innate immune responses across patients. In all cases, CellOT's accuracy and precision are superior to current state-of-the-art methods (Fig. **??**). Moreover, the predicted cell states after perturbation are still very close to the actually observed cell states. We consider these results as particularly promising, as it illustrates that accurate o.o.s. and o.o.d. predictions are indeed possible.

The ability to make predictions out-of-distribution, such as on unseen patients, is, however, only feasible if a) similar samples have been observed in the unperturbed setting, and b) the training set contains cases that are similar not only in their unperturbed state but also their perturbation response. An analysis of glioblastoma patients treated with Panobinostat (Zhao et al., 2021) (see **??**a-c) indeed confirms this restriction: CellOT and the baselines are able to predict treatment outcomes for those patients that are similar to other patients in both unperturbed state as well as perturbation effect (see Fig. **??**f), but fail to capture perturbation effects for

patients that exhibit unique responses (see **??**g). This limitation is important to consider when applying CellOT in o.o.d. settings. To overcome such problems, larger cohorts, additional meta-information, and methodological extensions are required. Bunne et al. (2022a) partially address this issue by deriving a neural optimal transport scheme that can be conditioned on a context, e.g., patient meta-data, when predicting perturbation responses.

We also observe that the predictive performance for CellOT drops when perturbations are too strong, i.e., the cell distributions before and after perturbations are very different (see Fig. **??**j); a similar drop is observed for the other methods (see **??**). The principle underlying the optimal transport theory is ideally suited for acute cellular perturbations during which single cells do not redistribute entirely and randomly in multidimensional measurement space, but typically only in a few dimensions, such that the overall correlation structure is preserved. While this modeling hypothesis is satisfied when perturbation responses are observed via regularly and frequently sampled snapshots, molecular transitions cannot be reconstructed when perturbation responses have progressed too far. For particularly strong or complicated perturbations, cellular multiplex profiles might change too drastically, violating OT assumptions and making it challenging to reconstruct the alignments between unperturbed and perturbed populations based on the *minimal effort* principle. In such settings, additional information is likely needed, for instance, a model of the underlying biology or models that integrate observations of multiple smaller time steps.

Despite the stochastic nature of cell fate decisions and the fact that cellular dynamics are intrinsically noisy (Wilkinson, 2009), CellOT models cell responses as deterministic trajectories. Approaches treating cell fate decisions as probabilistic events have previously allowed estimation of the full dynamical model to a greater extent than their deterministic counterparts (Bergen et al., 2020). By connecting OT and stochastic difference equations, recent work (Bunne et al., 2023; Somnath et al., 2023) can build up on CellOT to account for biological heteroscedasticity, at the cost of added model complexity and other simplifying assumptions.

Despite having provided a proof-of-concept of the capacity of CellOT to model various chemical perturbations for different data modalities through an in-depth analysis of the nature of the learned mapping as well as a demonstration of its versatility in a broad class of applications, CellOT's generalization capacity has been evaluated on relatively small datasets. Crucially, large cohorts comprised of patients with different molecular profiles, such as cancer patients with various underlying genetics, could

result in strongly heterogeneous treatment responses. It is evident that approaches addressing these challenges could readily exploit the upcoming availability of large-scale patient cohort studies. The use of neural optimal transport to learn single-cell drug responses makes thus for an exciting avenue for future work, including its use to improve our understanding of cell therapies, study drug responses from patient samples, and better account for cell-to-cell variability in large-scale drug design efforts.

BIBLIOGRAPHY

David Alvarez-Melis, Yair Schiff, and Youssef Mroueh. Optimizing Functionals on the Space of Probabilities with Input Convex Neural Networks. *arXiv Preprint arXiv:2106.00774*, 2021.

L. Ambrosio, N. Gigli, and G. Savaré. *Gradient Flows in Metric Spaces and in the Space of Probability Measures*. Springer, 2006.

Brandon Amos, Lei Xu, and J Zico Kolter. Input Convex Neural Networks. In *International Conference on Machine Learning (ICML)*, volume 34, 2017.

Martin Arjovsky, Soumith Chintala, and Léon Bottou. Wasserstein Generative Adversarial Networks. In *International Conference on Machine Learning (ICML)*. PMLR, 2017.

Jean-David Benamou, Guillaume Carlier, and Maxime Laborde. An augmented lagrangian approach to wasserstein gradient flows and applications. *ESAIM: Proceedings and surveys*, 54:1–17, 2016a.

Jean-David Benamou, Guillaume Carlier, Quentin Mérigot, and Edouard Oudet. Discretization of functionals involving the Monge–Ampére operator. *Numerische Mathematik*, 134(3), 2016b.

Volker Bergen, Marius Lange, Stefan Peidli, F Alexander Wolf, and Fabian J Theis. Generalizing RNA velocity to transient cell states through dynamical modeling. *Nature Biotechnology*, 38(12), 2020.

James Bradbury, Roy Frostig, Peter Hawkins, Matthew James Johnson, Chris Leary, Dougal Maclaurin, George Necula, Adam Paszke, Jake VanderPlas, Skye Wanderman-Milne, and Qiao Zhang. JAX: composable transformations of Python+NumPy programs, 2018. URL http://github.com/google/jax.

Yann Brenier. Décomposition polaire et réarrangement monotone des champs de vecteurs. *CR Acad. Sci. Paris Sér. I Math.*, 305, 1987.

Charlotte Bunne, Stefan G Stark, Gabriele Gut, Jacobo Sarabia del Castillo, Kjong-Van Lehmann, Lucas Pelkmans, Andreas Krause, and Gunnar Ratsch. Learning Single-Cell Perturbation Responses using Neural Optimal Transport. *bioRxiv*, 2021.

Charlotte Bunne, Andreas Krause, and Marco Cuturi. Supervised Training of Conditional Monge Maps. In *Advances in Neural Information Processing Systems (NeurIPS)*, 2022a.

Charlotte Bunne, Laetitia Meng-Papaxanthos, Andreas Krause, and Marco Cuturi. Proximal Optimal Transport Modeling of Population Dynamics. In *International Conference on Artificial Intelligence and Statistics (AISTATS)*, volume 25, 2022b.

Charlotte Bunne, Ya-Ping Hsieh, Marci Cuturi, and Andreas Krause. The Schrödinger Bridge between Gaussian Measures has a Closed Form. In *International Conference on Artificial Intelligence and Statistics (AISTATS)*, 2023.

Martin Burger, José A. Carrillo, and Marie-Therese Wolfram. A mixed finite element method for nonlinear diffusion equations. *Kinetic & Related Models*, 3(1), 2010.

Luis A Caffarelli. Monotonicity Properties of Optimal Transportation and the FKG and Related Inequalities. *Communications in Mathematical Physics*, 214(3), 2000.

Jose A Carrillo, Katy Craig, Li Wang, and Chaozhen Wei. Primal Dual Methods for Wasserstein Gradient Flows. *Foundations of Computational Mathematics*, 2021.

Rich Caruana. Multitask Learning. *Machine Learning*, 28(1), 1997.

Yash Chandak, Georgios Theocharous, James Kostas, Scott Jordan, and Philip Thomas. Learning Action Representations for Reinforcement Learning. In *International Conference on Machine Learning (ICML)*, 2019.

Tianrong Chen, Guan-Horng Liu, and Evangelos A Theodorou. Likelihood Training of Schrödinger Bridge using Forward-Backward SDEs Theory. In *International Conference on Learning Representations (ICLR)*, 2022a.

Wanze Chen, Orane Guillaume-Gentil, Pernille Yde Rainer, Christoph G Gäbelein, Wouter Saelens, Vincent Gardeux, Amanda Klaeger, Riccardo Dainese, Magda Zachara, Tomaso Zambelli, et al. Live-seq enables temporal transcriptomic recording of single cells. *Nature*, 608, 2022b.

Yize Chen, Yuanyuan Shi, and Baosen Zhang. Optimal Control Via Neural Networks: A Convex Approach. In *International Conference on Learning Representations (ICLR)*, 2019.

Yongxin Chen, Tryphon T Georgiou, and Michele Pavon. Optimal Transport in Systems and Control. *Annual Review of Control, Robotics, and Autonomous Systems*, 4, 2021a.

Yongxin Chen, Tryphon T Georgiou, and Michele Pavon. Stochastic control liaisons: Richard Sinkhorn meets Gaspard Monge on a Schrödinger bridge. *SIAM Review*, 63(2), 2021b.

Patrick L Combettes and Jean-Christophe Pesquet. Proximal splitting methods in signal processing. In *Fixed-point algorithms for inverse problems in science and engineering*, pages 185–212. Springer, 2011.

Gabriele Corso, Hannes Stärk, Bowen Jing, Regina Barzilay, and Tommi Jaakkola. Diffusion Steps, Twists, and Turns for Molecular Docking. In *International Conference on Learning Representations (ICLR)*, 2023.

Marco Cuturi. Sinkhorn Distances: Lightspeed Computation of Optimal Transport. In *Advances in Neural Information Processing Systems (NeurIPS)*, volume 26, 2013.

Marco Cuturi, Laetitia Meng-Papaxanthos, Yingtao Tian, Charlotte Bunne, Geoff Davis, and Olivier Teboul. Optimal Transport Tools (OTT): A JAX Toolbox for all things Wasserstein. *arXiv Preprint arXiv:2201.12324*, 2022.

John M Danskin. *The Theory of Max-Min and its Applications to Weapons Allocation Problems*, volume 5. Springer, 1967.

Gwendoline De Bie, Gabriel Peyré, and Marco Cuturi. Stochastic Deep Networks. In *International Conference on Machine Learning (ICML)*, volume 36, 2019.

Valentin De Bortoli, James Thornton, Jeremy Heng, and Arnaud Doucet. Diffusion schrödinger bridge with applications to score-based generative modeling. In *Advances in Neural Information Processing Systems (NeurIPS)*, volume 34, 2021.

Atray Dixit, Oren Parnas, Biyu Li, Jenny Chen, Charles P Fulco, Livnat Jerby-Arnon, Nemanja D Marjanovic, Danielle Dionne, Tyler Burks, Raktima Raychowdhury, et al. Perturb-Seq: Dissecting Molecular Circuits with Scalable Single-Cell RNA Profiling of Pooled Genetic Screens. *Cell*, 167 (7), 2016.

D. C. Dowson and B. V. Landau. The Fréchet distance between multivariate normal distributions. *Journal of Multivariate Analysis*, 12(3), 1982.

Harrison Edwards and Amos Storkey. Towards a Neural Statistician. In *International Conference on Learning Representations (ICLR)*, volume 5, 2017.

Jiaojiao Fan, Amirhossein Taghvaei, and Yongxin Chen. Scalable Computations of Wasserstein Barycenter via Input Convex Neural Networks. In *International Conference on Machine Learning (ICML)*, 2021.

Jean Feydy, Thibault Séjourné, François-Xavier Vialard, Shun-Ichi Amari, Alain Trouvé, and Gabriel Peyré. Interpolating between Optimal Transport and MMD using Sinkhorn Divergences. In *International Conference on Artificial Intelligence and Statistics (AISTATS)*, volume 22, 2019.

Alessio Figalli. The Optimal Partial Transport Problem. *Archive for Rational Mechanics and Analysis*, 195(2), 2010.

Mike Fisher, Jorge Nocedal, Yannick Trémolet, and Stephen J Wright. Data assimilation in weather forecasting: a case study in pde-constrained optimization. *Optimization and Engineering*, 10(3):409–426, 2009.

Rémi Flamary, Nicolas Courty, Alexandre Gramfort, Mokhtar Z. Alaya, Aurélie Boisbunon, Stanislas Chambon, Laetitia Chapel, Adrien Corenflos, Kilian Fatras, Nemo Fournier, Léo Gautheron, Nathalie T.H. Gayraud, Hicham Janati, Alain Rakotomamonjy, Ievgen Redko, Antoine Rolet, Antony Schutz, Vivien Seguy, Danica J. Sutherland, Romain Tavenard, Alexander Tong, and Titouan Vayer. POT: Python Optimal Transport. *Journal of Machine Learning Research*, 22, 2021.

Chris J Frangieh, Johannes C Melms, Pratiksha I Thakore, Kathryn R Geiger-Schuller, Patricia Ho, Adrienne M Luoma, Brian Cleary, Livnat Jerby-Arnon, Shruti Malu, Michael S Cuoco, et al. Multimodal pooled Perturb-CITE-seq screens in patient models define mechanisms of cancer immune evasion. *Nature Genetics*, 53(3):332–341, 2021.

Matthias Gelbrich. On a Formula for the L^2 Wasserstein Metric between Measures on Euclidean and Hilbert Spaces. *Mathematische Nachrichten*, 147(1), 1990.

Arthur Gretton, Karsten M Borgwardt, Malte J Rasch, Bernhard Schölkopf, and Alexander Smola. A Kernel Two-Sample Test. *Journal of Machine Learning Research*, 13, 2012.

David Ha, Andrew Dai, and Quoc V Le. Hypernetworks. *arXiv preprint arXiv:1609.09106*, 2016.

Tatsunori Hashimoto, David Gifford, and Tommi Jaakkola. Learning Population-Level Diffusions with Generative Recurrent Networks. In *International Conference on Machine Learning (ICML)*, volume 33, 2016.

Lars Holdijk, Yuanqi Du, Ferry Hooft, Priyank Jaini, Bernd Ensing, and Max Welling. Path integral stochastic optimal control for sampling transition paths. *arXiv preprint arXiv:2207.02149*, 2022.

Chin-Wei Huang, Ricky T. Q. Chen, Christos Tsirigotis, and Aaron Courville. Convex Potential Flows: Universal Probability Distributions with Optimal Transport and Convex Optimization. In *International Conference on Learning Representations (ICLR)*, 2021.

Jan-Christian Hütter and Philippe Rigollet. Minimax estimation of smooth optimal transport maps. *The Annals of Statistics*, 49(2), 2021.

Leygonie Jacob, Jennifer She, Amjad Almahairi, Sai Rajeswar, and Aaron Courville. W2GAN: Recovering an Optimal Transport Map with a GAN. In *arXiv Preprint*, 2018.

Hicham Janati, Thomas Bazeille, Bertrand Thirion, Marco Cuturi, and Alexandre Gramfort. Multi-subject MEG/EEG source imaging with sparse multi-task regression. *NeuroImage*, 220, 2020.

Richard Jordan, David Kinderlehrer, and Felix Otto. The Variational Formulation of the Fokker–Planck Equation. *SIAM Journal on Mathematical Analysis*, 29(1), 1998.

Diederik P Kingma and Jimmy Ba. Adam: A Method for Stochastic Optimization. In *International Conference on Learning Representations (ICLR)*, 2014.

Peter E Kloeden and Eckhard Platen. Stochastic Differential Equations. In *Numerical Solution of Stochastic Differential Equations*. Springer, 1992.

Alexander Korotin, Vage Egiazarian, Arip Asadulaev, Alexander Safin, and Evgeny Burnaev. Wasserstein-2 Generative Networks. In *International Conference on Learning Representations (ICLR)*, 2020.

Alexander Korotin, Lingxiao Li, Aude Genevay, Justin M Solomon, Alexander Filippov, and Evgeny Burnaev. Do Neural Optimal Transport Solvers Work? A Continuous Wasserstein-2 Benchmark. *Advances in Neural Information Processing Systems (NeurIPS)*, 34, 2021.

Shivanni Kummar, Helen X Chen, John Wright, Susan Holbeck, Myrtle Davis Millin, Joseph Tomaszewski, James Zweibel, Jerry Collins, and James H Doroshow. Utilizing targeted cancer therapeutic agents in combination: novel approaches and urgent requirements. *Nature Reviews Drug discovery*, 9(11), 2010.

E Kun, YTM Tsang, CW Ng, DM Gershenson, and KK Wong. MEK inhibitor resistance mechanisms and recent developments in combination trials. *Cancer Treatment Reviews*, 92:102137, 2021.

Hugo Lavenant, Stephen Zhang, Young-Heon Kim, and Geoffrey Schiebinger. Towards a mathematical theory of trajectory inference. *arXiv preprint arXiv:2102.09204*, 2021.

Guan-Horng Liu, Tianrong Chen, Oswin So, and Evangelos A Theodorou. Deep Generalized Schrödinger Bridge. In *Advances in Neural Information Processing Systems (NeurIPS)*, 2022.

Romain Lopez, Jeffrey Regier, Michael B Cole, Michael I Jordan, and Nir Yosef. Deep generative modeling for single-cell transcriptomics. *Nature methods*, 15(12), 2018.

Jonathan Lorraine, Paul Vicol, and David Duvenaud. Optimizing Millions of Hyperparameters by Implicit Differentiation. In *International Conference on Artificial Intelligence and Statistics (AISTATS)*, 2020.

Mohammad Lotfollahi, F Alexander Wolf, and Fabian J Theis. scGen predicts single-cell perturbation responses. *Nature Methods*, 16(8), 2019.

Mohammad Lotfollahi, Anna Klimovskaia Susmelj, Carlo De Donno, Yuge Ji, Ignacio L Ibarra, F Alexander Wolf, Nafissa Yakubova, Fabian J Theis, and David Lopez-Paz. Compositional perturbation autoencoder for single-cell response modeling. *bioRxiv*, 2021.

Ashok Makkuva, Amirhossein Taghvaei, Sewoong Oh, and Jason Lee. Optimal transport mapping via input convex neural networks. In *International Conference on Machine Learning (ICML)*, volume 37, 2020.

Robert J McCann. A Convexity Principle for Interacting Gases. *Advances in Mathematics*, 128(1), 1997.

Leland McInnes, John Healy, and James Melville. UMAP: Uniform Manifold Approximation and Projection for Dimension Reduction. *arXiv Preprint*, 2018.

Luke Metz, Ben Poole, David Pfau, and Jascha Sohl-Dickstein. Unrolled Generative Adversarial Networks. In *International Conference on Learning Representations (ICLR)*, 2017.

Reza Bayat Mokhtari, Tina S Homayouni, Narges Baluch, Evgeniya Morgatskaya, Sushil Kumar, Bikul Das, and Herman Yeger. Combination therapy in combating cancer. *Oncotarget*, 8(23):38022, 2017.

Petr Mokrov, Alexander Korotin, Lingxiao Li, Aude Genevay, Justin Solomon, and Evgeny Burnaev. Large-Scale Wasserstein Gradient Flows. *Advances in Neural Information Processing Systems (NeurIPS)*, 2021.

Gaspard Monge. Mémoire sur la théorie des déblais et des remblais. *Histoire de l'Académie Royale des Sciences*, pages 666–704, 1781.

Kevin R Moon, David van Dijk, Zheng Wang, Scott Gigante, Daniel B Burkhardt, William S Chen, Kristina Yim, Antonia van den Elzen, Matthew J Hirn, Ronald R Coifman, et al. Visualizing structure and transitions in high-dimensional biological data. *Nature Biotechnology*, 37 (12), 2019.

Thomas M Norman, Max A Horlbeck, Joseph M Replogle, Alex Y Ge, Albert Xu, Marco Jost, Luke A Gilbert, and Jonathan S Weissman. Exploring genetic interaction manifolds constructed from rich single-cell phenotypes. *Science*, 365(6455), 2019.

François-Pierre Paty, Alexandre d'Aspremont, and Marco Cuturi. Regularity as Regularization: Smooth and Strongly Convex Brenier Potentials in Optimal Transport. In *International Conference on Artificial Intelligence and Statistics (AISTATS)*, 2020.

Gabriel Peyré. Entropic Approximation of Wasserstein Gradient Flows. *SIAM Journal on Imaging Sciences*, 8(4), 2015.

Gabriel Peyré and Marco Cuturi. Computational Optimal Transport. *Foundations and Trends in Machine Learning*, 11(5-6), 2019. ISSN 1935-8245.

Aram-Alexandre Pooladian and Jonathan Niles-Weed. Entropic estimation of optimal transport maps. *arXiv preprint arXiv:2109.12004*, 2021.

Neha Prasad, Karren Yang, and Caroline Uhler. Optimal Transport using GANs for Lineage Tracing. *arXiv preprint arXiv:2007.12098*, 2020.

Aaditya Ramdas, Nicolás García Trillos, and Marco Cuturi. On Wasserstein Two Sample Testing and Related Families of Nonparametric Tests. *Entropy*, 19(2):47, 2017.

Jack Richter-Powell, Jonathan Lorraine, and Brandon Amos. Input Convex Gradient Networks. *arXiv preprint arXiv:2111.12187*, 2021.

Philippe Rigollet and Austin J Stromme. On the sample complexity of entropic optimal transport. *arXiv preprint arXiv:2206.13472*, 2022.

David Rogers and Mathew Hahn. Extended-Connectivity Fingerprints. *Journal of Chemical Information and Modeling*, 50(5), 2010.

Yu Rong, Yatao Bian, Tingyang Xu, Weiyang Xie, Ying Wei, Wenbing Huang, and Junzhou Huang. Self-Supervised Graph Transformer on Large-Scale Molecular Data. *Advances in Neural Information Processing Systems (NeurIPS)*, 2020.

Tim Salimans, Han Zhang, Alec Radford, and Dimitris Metaxas. Improving GANs Using Optimal Transport. In *International Conference on Learning Representations (ICLR)*, 2018.

Filippo Santambrogio. Optimal Transport for Applied Mathematicians. *Birkhäuser, NY*, 55(58-63):94, 2015.

Filippo Santambrogio. {Euclidean, metric, and Wasserstein} gradient flows: an overview. *Bulletin of Mathematical Sciences*, 7(1), 2017.

Kevin Scaman and Aladin Virmaux. Lipschitz regularity of deep neural networks: analysis and efficient estimation. In *Advances in Neural Information Processing Systems (NeurIPS)*, 2018.

Geoffrey Schiebinger, Jian Shu, Marcin Tabaka, Brian Cleary, Vidya Subramanian, Aryeh Solomon, Joshua Gould, Siyan Liu, Stacie Lin, Peter Berube, et al. Optimal-Transport Analysis of Single-Cell Gene Expression Identifies Developmental Trajectories in Reprogramming. *Cell*, 176(4), 2019a.

Geoffrey Schiebinger, Jian Shu, Marcin Tabaka, Brian Cleary, Vidya Subramanian, Aryeh Solomon, Joshua Gould, Siyan Liu, Stacie Lin, Peter Berube, et al. Optimal-Transport Analysis of Single-Cell Gene Expression Identifies Developmental Trajectories in Reprogramming. *Cell*, 176(4), 2019b.

Morgan A Schmitz, Matthieu Heitz, Nicolas Bonneel, Fred Ngole, David Coeurjolly, Marco Cuturi, Gabriel Peyré, and Jean-Luc Starck. Wasserstein dictionary learning: Optimal transport-based unsupervised nonlinear dictionary learning. *SIAM Journal on Imaging Sciences*, 11(1):643–678, 2018.

Erwin Schrödinger. *Über die Umkehrung der Naturgesetze*. Verlag der Akademie der Wissenschaften in Kommission bei Walter De Gruyter u. Company, 1931.

Philippe Schwaller, Alain C Vaucher, Ruben Laplaza, Charlotte Bunne, Andreas Krause, Clemence Corminboeuf, and Teodoro Laino. Machine intelligence for chemical reaction space. *Wiley Interdisciplinary Reviews: Computational Molecular Science*, page e1604, 2022.

Vignesh Ram Somnath, Matteo Pariset, Ya-Ping Hsieh, Maria Rodriguez Martinez, Andreas Krause, and Charlotte Bunne. Aligned Diffusion Schrödinger Bridges. In *Conference on Uncertainty in Artificial Intelligence (UAI)*, 2023.

Yang Song, Jascha Sohl-Dickstein, Diederik P Kingma, Abhishek Kumar, Stefano Ermon, and Ben Poole. Score-Based Generative Modeling through Stochastic Differential Equations. In *International Conference on Learning Representations (ICLR)*, 2021.

Sanjay R Srivatsan, Jose L McFaline-Figueroa, Vijay Ramani, Lauren Saunders, Junyue Cao, Jonathan Packer, Hannah A Pliner, Dana L Jackson, Riza M Daza, Lena Christiansen, et al. Massively multiplex chemical transcriptomics at single-cell resolution. *Science*, 367(6473), 2020.

Guy Tennenholtz and Shie Mannor. The Natural Language of Actions. In *International Conference on Machine Learning (ICML)*, 2019.

Alexander Tong, Jessie Huang, Guy Wolf, David Van Dijk, and Smita Krishnaswamy. TrajectoryNet: A Dynamic Optimal Transport Network for Modeling Cellular Dynamics. In *International Conference on Machine Learning (ICML)*, 2020.

Alexander Tong, Nikolay Malkin, Guillaume Huguet, Yanlei Zhang, Jarrid Rector-Brooks, Kilian Fatras, Guy Wolf, and Yoshua Bengio. Conditional Flow Matching: Simulation-Free Dynamic Optimal Transport. *arXiv preprint arXiv:2302.00482*, 2023.

Alexa B Turke, Youngchul Song, Carlotta Costa, Rebecca Cook, Carlos L Arteaga, John M Asara, and Jeffrey A Engelman. MEK inhibition leads to PI3K/AKT activation by relieving a negative feedback on ERBB receptors. *Cancer Research*, 72(13), 2012.

Francisco Vargas, Pierre Thodoroff, Neil D Lawrence, and Austen Lamacraft. Solving Schrödinger Bridges via Maximum Likelihood. *Entropy*, 23(9), 2021.

Ashish Vaswani, Noam Shazeer, Niki Parmar, Jakob Uszkoreit, Llion Jones, Aidan N Gomez, Łukasz Kaiser, and Illia Polosukhin. Attention is All you Need. In *Advances in Neural Information Processing Systems (NeurIPS)*, 2017.

Cédric Villani. *Optimal transport: old and new*, volume 338. Springer, 2009.

Caleb Weinreb, Alejo Rodriguez-Fraticelli, Fernando D Camargo, and Allon M Klein. Lineage tracing on transcriptional landscapes links state to fate during differentiation. *Science*, 367(6479), 2020.

Darren J Wilkinson. Stochastic modelling for quantitative description of heterogeneous biological systems. *Nature Reviews Genetics*, 10(2), 2009.

Ronald J Williams and David Zipser. A Learning Algorithm for Continually Running Fully Recurrent Neural Networks. *Neural Computation*, 1(2), 1989.

Karren D Yang and Caroline Uhler. Scalable Unbalanced Optimal Transport using Generative Adversarial Networks. *International Conference on Learning Representations (ICLR)*, 2019.

Karren Dai Yang, Karthik Damodaran, Saradha Venkatachalapathy, Ali C Soylemezoglu, GV Shivashankar, and Caroline Uhler. Predicting cell lineages using autoencoders and optimal transport. *PLoS Computational Biology*, 16(4), 2020.

Manzil Zaheer, Satwik Kottur, Siamak Ravanbakhsh, Barnabas Poczos, Russ R Salakhutdinov, and Alexander J Smola. Deep Sets. In *Advances in Neural Information Processing Systems (NeurIPS)*, volume 30, 2017.

Wenting Zhao, Athanassios Dovas, Eleonora Francesca Spinazzi, Hanna Mendes Levitin, Matei Alexandru Banu, Pavan Upadhyayula, Tejaswi Sudhakar, Tamara Marie, Marc L Otten, Michael B Sisti, et al. Deconvolution of cell type-specific drug responses in human tumor tissue with single-cell RNA-seq. *Genome Medicine*, 13(1), 2021.

CURRICULUM VITAE

PERSONAL DATA

Name	Charlotte Bunne
Date of Birth	August 29, 1995
Place of Birth	Karlsruhe, Germany
Citizen of	Germany

EDUCATION

2022-2023	Broad Institute of MIT and Harvard, Cambridge (MA), USA Visiting Graduate Student
2016 – 2019	Eidgenössische Technische Hochschule (ETH), Zürich, Switzerland *Final Degree:* Master of Science
2018-2019	Massachusetts Institute of Technology (MIT), Cambridge (MA), USA Visiting Student
2013 – 2016	Heidelberg University Heidelberg, Germany *Final Degree:* Bachelor of Science

EMPLOYMENT

2022	Research Intern *Apple*, Paris, France
2020	Research Intern *Google Research*, Zürich, Switzerland
2017	Research Intern *IBM Research*, Zürich, Switzerland

PUBLICATIONS

Charlotte Bunne, Andreas Krause, and Marco Cuturi. Supervised Training of Conditional Monge Maps. In *Advances in Neural Information Processing Systems (NeurIPS)*, 2022.

A

APPENDIX

Here be dragons.